HydroQuantum: A new quantum-driven Python package for hydrological simulation

Mostafa Saberian [a], Nima Zafarmomen [b], Adarsha Neupane [b], Krishna Panthi [c], Vidya Samadi [b,d,*]

[a] *The Glenn Department of Civil Engineering, Clemson University, Clemson, SC, USA*
[b] *Department of Agricultural Sciences, Clemson University, Clemson, SC, USA*
[c] *School of Computing, Clemson University, Clemson, SC, USA*
[d] *Artificial Intelligence Research Institute for Science and Engineering (AIRISE), School of Computing, Clemson University, SC, USA*

ARTICLE INFO

ABSTRACT

This research aims to leverage the power of quantum computing for hydrological simulation. A new "Hydro-Quantum" Python package is created to facilitate this implementation, enabling researchers to explore the potential of quantum algorithms in hydrological simulations. "HydroQuantum" was implemented for daily streamflow and stream water temperature (SWT) simulations across continental US. The package includes Variational Quantum Circuits (VQC), a fully quantum Long Short-Term Memory network (QLSTM), and a hybrid quantum-classical LSTM. All algorithms were benchmarked against classical LSTM and trained and tested during 2000–2014 and 2015–2022 for daily streamflow and SWT simulations, respectively. While QLSTM showed impressive results in capturing temporal dependencies in streamflow data, it consistently underperformed classical LSTM for SWT simulation. Sensitivity analysis further revealed that precipitation and snow-water equivalent were two major contributors to quantum-driven simulation. This research explores the potential of quantum computing in complex time series simulations, leading to breakthroughs in hydrological modeling.

1. Introduction

Understanding the variability of streamflow and stream water temperature (SWT) is essential for effective water resource management, especially in areas with high water demand, drought and flood-prone regions, and those areas experiencing impacts of climate change (e.g., Hamlet et al., 2002; Samadi et al., 2025). Both streamflow and SWT are vital hydrological variables for the sustainable management of freshwater systems that can serve as key indicators for water quantity and quality conditions. Accurate assessment of both variables is therefore vital for efficient water allocation, improving resilience to extreme hydrological events (Okewu et al., 2017; Zafarmomen and Samadi, 2025), and maintaining ecologically healthy aquatic habitats (He et al., 2024).

Deterministic and physics-based hydrological models have long been used to simulate streamflow and SWT (Vliet et al., 2012; Zafarmomen et al., 2024). To name a few examples, models such as Hydrologiska Byrans Vattenavdelning (HBV; Bergström, 1976), TOPMODEL (Beven and Kirkby, 1979), and WRF-Hydro (Gochis et al., 2015) are commonly applied for streamflow simulation, while SNTemp (Bartholow, 1989)

and SHADE-HSPE (Chen et al., 1998) are among the tools used for SWT modeling. In addition, Soil and Water Assessment Tool (SWAT; Arnold et al., 1998) and Hydrological Simulation Program - FORTRAN (HSPF; Bicknell et al., 1997) are two well-known physical based models used to simulate both streamflow and SWT. These models rely on complex mathematical formulations and extensive physical parameters to simulate hydrological processes (Fathian et al., 2019; Lei et al., 2024). Additionally, classical statistical approaches such as Autoregressive Moving Average (ARMA; Mohammadi et al., 2006; Bosompemaa et al., 2025), Autoregressive Integrated Moving Average (ARIMA; Wen et al., 2019), and linear regression (LR; Ulaski et al., 2023) have been employed as more computationally efficient alternatives for streamflow and SWT simulations. However, like physics-based models, they often fall short in capturing the nonlinear, nonstationary, and complex interactions inherent in hydrological processes (Wang et al., 2021).

In contrast, machine learning methods, including Support Vector Regression (SVR; Yu et al., 2018; Hani et al., 2023), Artificial Neural Networks (ANN; Tan et al., 2018; Graf and Aghelpour, 2021), and Random Forest (RF; Oppel and Schumann, 2020; Neupane and Sawada,

---

2023), offer greater flexibility for modeling nonlinear and nonstationary patterns in streamflow and SWT data. Recently, more complex machine learning models have also been implemented in this domain (Kratzert et al., 2018; Saberian et al., 2024; Umutoni et al., 2025), further advancing predictive capabilities of streamflow and SWT simulations. Among these, Long Short-Term Memory (LSTM; Hochreiter and Schmidhuber, 1997), a variant of Recurrent Neural Network (RNN), has shown strong performance in capturing long-term temporal dependencies in data (Gers et al., 2000). Coupling LSTM with other data-driven algorithms (hybrid configurations) such as LSTM-SVR (Dehghani et al., 2023), Convolutional Neural Network-LSTM (Ghimire et al., 2021; Windheuser et al., 2023), and LSTM-Deep Neural Network (LSTM-DNN; Lin et al., 2023) have further improved predictive performance of streamflow and SWT. For example, Rahmani et al. (2021) applied LSTM for daily SWT simulation across >400 data-sparse and unmonitored basins in the contiguous U.S. (CONUS), achieving robust results. Building on these findings, Sadler et al. (2022) applied a multitask LSTM to predict both streamflow and SWT simultaneously, where multitask learning either enhanced accuracy or performed on par with single-task models. Despite these advancements, LSTMs are susceptible to the vanishing-gradient problem, where gradients can potentially destabilize the training process (Tabas and Samadi, 2022; Xu et al., 2024; Zhou et al., 2024).

The emergence of quantum computing offers transformative potential to overcome the limitations of classical DNN such as LSTMs. Quantum computing, which leverages superposition and entanglement, enables parallel processing and efficient handling of high-dimensional data (e.g., Wang, 2012). Superposition enables quantum bits (qubits) to exist in multiple states simultaneously, while entanglement links qubits so that their states remain correlated regardless of distance (Forcer et al., 2002; Simoes et al., 2023). These features enhance the representational power and computational efficiency of predictive models (Khan et al., 2024; Dutta et al., 2024). Quantum neural network, which integrates quantum principles with classical machine learning, has shown significant promise in time series simulations (Innan et al., 2024; Sakhuja et al., 2025). They excel in addressing complex data-driven challenges, making these techniques powerful tools for various simulation tasks (Biamonte et al., 2017).

The goal of this study is to develop a new quantum computing Python package called "HydroQuantum" for daily streamflow and SWT simulations. The package includes Quantum LSTM (QLSTM), a hybrid quantum-classical LSTM, and Variational Quantum Circuit (VQC). These approaches were implemented for streamflow and SWT simulation across CONUS. Quantum LSTM (QLSTM) extends classical LSTM by incorporating VQCs within its architecture, replacing traditional neural network components in the LSTM cells (Chen et al., 2022). This enhancement enables faster convergence and improves the simulation of temporal dependencies inherent in time series data (Sai et al., 2024).

Alongside QLSTM, we also implemented a hybrid quantum-classical LSTM and VQC that leveraged both classical and quantum computing components for processing sequential data. Unlike QLSTM, which fully replaces traditional neural network layers with quantum circuits, hybrid quantum-classical LSTM introduces a quantum layer alongside classical LSTM layers, creating a synergistic architecture designed to extract richer temporal features in time series data. VQC, on other hand, employs parameterized quantum circuits for time series simulation which are then optimized using classical optimization algorithms. This process represents a fundamental step in quantum machine learning where classical data is transformed into a quantum state, manipulated by quantum circuits, and then measured to assess the results. The classical optimizer then refines the parameters of the quantum circuits to minimize a loss function and effectively train the algorithm.

Despite the promise of quantum neural networks, its application in hydrological simulation remains largely unexplored. This study is the first known attempt by the authors to bridge this gap by implementing multiple quantum-driven algorithms in simulating hydrological variables such as daily streamflow and SWT. The objectives of this research are to: (i) investigate the efficacy of QLSTM, VQC, and hybrid quantum-classical LSTM in addressing nonlinear and nonstationary relationships in daily streamflow and SWT simulations; (ii) compare the performance of QLSTM, VQC, and hybrid quantum-classical LSTM with classical LSTM in terms of simulation accuracy and performance; (iii) conduct a region-specific sensitivity analysis that identifies the importance of key meteorological predictors, highlighting the influence of each climatic variable on quantum-driven modeling performance; and (iv) examine the model's capacity for spatial generalization by testing its ability to simulate streamflow at unseen locations within the same hydrological region; and (v) integrating all these proposed quantum-driven algorithms in a new Python package—called HydroQuantum. By advancing the use of quantum computing within the domain of streamflow and SWT simulation, this work aims to lay the foundation for more accurate, efficient, and scalable quantum-driven algorithms for hydrological applications.

The remainder of this paper is organized as follows: Section 2 describes the study area and dataset and introduces the fundamentals of quantum computing and the workflow of proposed models. Section 3 presents the results and discussion, including performance evaluation, sensitivity analysis, and model generalization for different hydrological regions across CONUS. Finally, Section 5 concludes the results and provides recommendations for future research.

2. Methodology

2.1. Study area and data

This study used publicly available Catchment Attributes and Meteorology for Large-sample Studies (CAMELS) for daily streamflow data which was curated by the National Center for Atmospheric Research (NCAR; Newman et al., 2015). CAMELS consists of 18 large basins (Hydrologic Unit Code 2; HUC2) or zones containing a total of 671 catchments (HUC8) ranging in size from 4 to 25,000 km^2 (Fig. 1). These catchments were selected based on their minimal human intervention and long-term data records (1980–2014) gathered from the United States Geological Survey (USGS) Gauge II stations and the National Water Information System (NWIS). In addition, CAMELS includes daily meteorological forcing data from Daymet (Thornton et al., 2016), and the North American Land Data Assimilation System (NLDAS; Xia et al., 2014). Daymet provides long-term, continuous, gridded estimates of daily weather and climatology variables. The Maurer dataset is a model-derived dataset of land surface states and fluxes, and NLDAS is a quality-controlled, spatially and temporally consistent, land-surface model (LSM) dataset. CAMELS also includes several catchment physical attributes related to soil, climate, vegetation, topography, and geology (Addor et al., 2017). These catchment attributes were derived from maps, remote sensing products, and climate data that are generally available across CONUS.

For this study, we used 394 of the 671 CAMELS catchments (those with an area of <2000 km^2) categorized as the USGS Gauge-II stations; these 394 catchments were among those used for model benchmarking by Newman et al. (2017). Fig. 1 shows the CAMELS basins within the HUC2 zones and the USGS gauging stations used in this study. This study also employed the meteorological forcing data as time-dependent parameters. Time-dependent parameters include variables that change over time, such as: (i) daily precipitation (prcp [mm/day]), (ii) minimum daily air temperature (tmin [°C]), (iii) maximum daily air temperature (tmax [°C]), (iv) mean short-wave radiation ($srad$ [W/m^2]), (v) vapor pressure (vp [Pa]), and (vi) snow water equivalent (swe [mm]).

2.1.1. SWT data
SWT data were collected from the USGS WaterWatch (2025) gauge II stations. We created SWT datasets for 27 gauging stations across CONUS (see Fig. 1). Meteorological forcing data were derived from the NLDAS
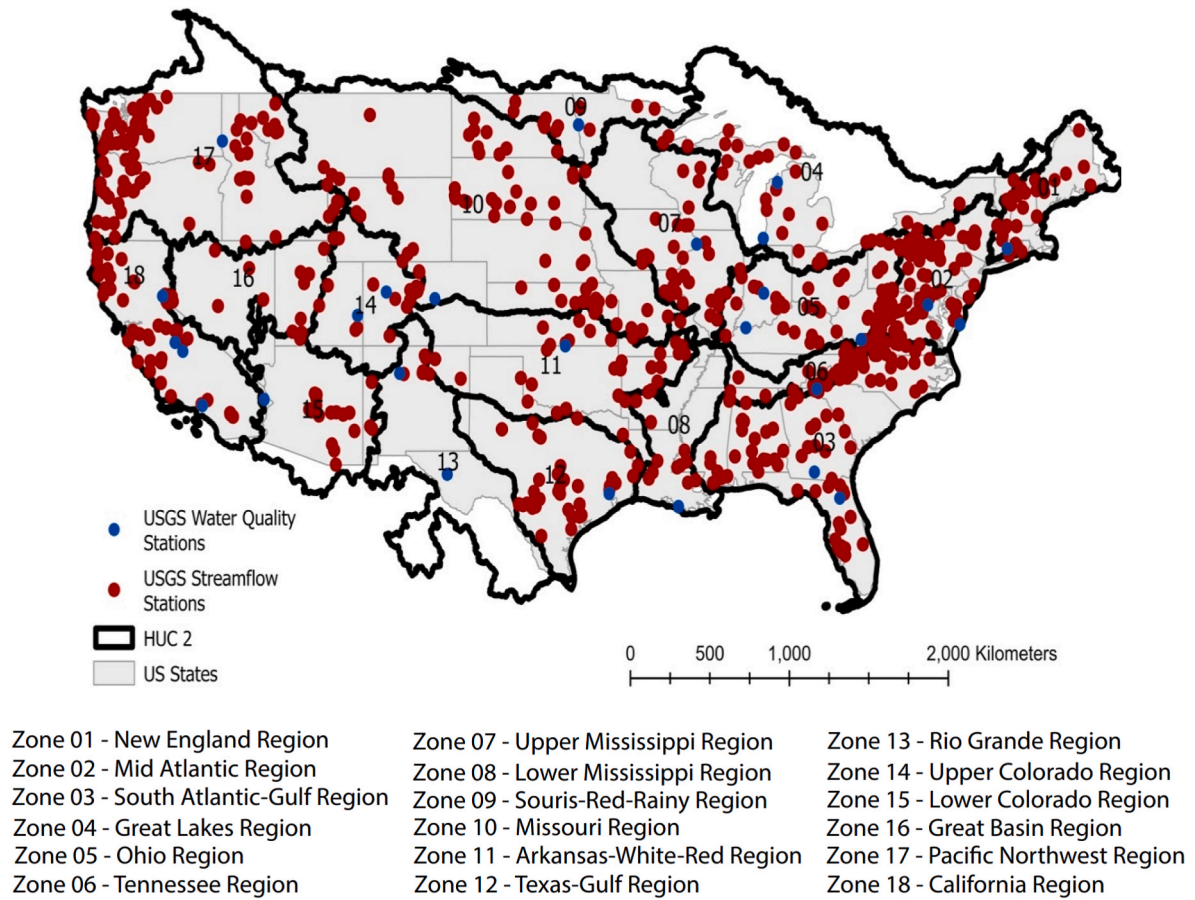
Fig. 1. Distribution of 18 CAMELS HUC2 (or zones) across CONUS. The USGS streamflow (red dots) and SWT (blue dots) for gauge II stations correspond to major HUC2 basins. These stations were selected based on data continuity and regional representativeness within each zone. (For interpretation of the references to colour in this figure legend, the reader is referred to the Web version of this article.)

dataset to simulate SWT. We utilized daily NLDAS outputs corresponding to 27 stations. This subset covered the temporal period from October 1, 2015 to September 30, 2022 and provided the necessary climatic variables for subsequent SWT modeling.

The NLDAS variables serve as the predictor features for simulating the next day SWT. These features include: (i) daily total precipitation (mm/day), (ii) daily mean air temperature (Kelvin), (iii) daily mean specific humidity (kg/kg), (iv) daily mean zonal wind speed (m/s), (v) daily mean meridional wind speed (m/s), (vi) daily mean surface downwelling shortwave radiation (W/m^2), (vii) daily mean surface downwelling longwave radiation (W/m^2), and (viii) daily mean potential evapotranspiration (mm/day). These parameters, representing the atmospheric conditions on a given day (t), were used as input to predict the water temperature ($°C$) on the subsequent day ($t+1$).

2.1.2. Data preprocessing

Prior to model implementation, we applied a quality control approach to exclude catchments with excessive data gaps. Specifically, catchments with more than 30 consecutive days of missing data were excluded. This threshold was selected because the model uses a lookback window of 30 days, and longer missing sequences would disrupt the temporal input continuity required for training. The analysis focused on the period from October 1, 2000, to September 30, 2014. After applying these criteria, a total of 394 catchments with sufficient data continuity were selected for daily streamflow simulation. To address shorter data gaps (fewer than 30 consecutive days), a linear interpolation was applied to ensure continuity in the input sequences. The resulting dataset was divided into training and validation sets covering the first ten years (October 1, 2000, to October 1, 2010), and a testing set

spanning the subsequent four years (October 2, 2010, to September 30, 2014), to evaluate modeling performance.

For the SWT simulation, we began with data from 41 stations covering the period 2013–2025, which contained significant missing values. To maximize the number of stations suitable for modeling, we selected a specific multi-year period that minimized continuous missing data stretches. Specifically, we aimed to identify a period when the maximum number of stations had fewer than 30 consecutive days of missing data. The 30-day threshold was chosen based on the lookback window used in our analysis. This window length was selected because previous studies (Sun et al., 2021) demonstrated the adequacy of this method for next-day prediction tasks. This approach resulted in 27 stations with continuous data of 7 years from October 1, 2015, to September 30, 2022. Any remaining missing values within the data for these 27 stations during this seven-year period were then filled using simple linear regression. Subsequently, the dataset was divided into a training and validation set covering five years (October 1, 2015, to October 1, 2020), and a testing set covering two years of the data (October 2, 2020, to September 30, 2022).

2.2. Quantum computing approaches

2.2.1. Quantum bit

In classical computing, the smallest unit of information is a bit, which can exist in one of two states: 0 or 1. In contrast, the smallest unit of information in quantum computing is called a qubit (quantum bit). A qubit (Nielsen and Chuang, 2010) can exist not only in the states analogous to classical 0 and 1, but also in a superposition of these states. The two bits are represented as vectors $|0\rangle$ and $|1\rangle$, and are called the basis

states. Mathematically, a general qubit is represented as a linear combination of the basis states:

$$|\psi\rangle = a|0\rangle + b|1\rangle \qquad \text{(Equation 1)}$$

where, a and b are complex numbers called probability amplitudes. The state of a qubit is normalized, meaning the sum of the squares of the amplitudes must equal 1, i.e., $|a|^2 + |b|^2 = 1$. When a qubit is measured, it collapses to one of the basis states. The probability of measuring a qubit as $|0\rangle$ is given by $|a|^2$ (the squared magnitude of a), and the probability of measuring it as $|1\rangle$ is given by $|b|^2$ (the squared magnitude of b). A qubit can be visualized using a representation called the Bloch sphere (Nielsen and Chuang, 2010) where the amplitudes a and b determine a point on the surface of a unit sphere.

2.2.2. Bloch sphere

Since a and b are complex numbers, they can be represented in polar form as

$$|\psi\rangle = |a|e^{i\gamma}|0\rangle + |b|e^{i\delta}|1\rangle \qquad \text{(Equation 2)}$$

$$|\psi\rangle = e^{i\gamma}\left(|a||0\rangle + |b|e^{i\phi}|1\rangle\right) \qquad \text{(Equation 3)}$$

Let $\phi = \delta - \gamma$ represent the relative phase between $|0\rangle$ and $|1\rangle$. Since $|a|^2 + |b|^2 = 1$, we can define an angle ω such that: $|a| = cos\left(\frac{\omega}{2}\right)$ and $|b| = \sin\left(\frac{\omega}{2}\right)$.

The factor $e^{i\gamma}$ is a global phase. It doesn't affect the probabilities of measuring $|0\rangle$ and $|1\rangle$ and is considered physically irrelevant for a single qubit (Nielsen and Chuang, 2010).

This means, a qubit can be represented using ω, which determines the probabilities of measuring $|0\rangle$ and $|1\rangle$ and ϕ which represents the relative phase. A Bloch sphere is a unit sphere in complex space where ω and ϕ are the spherical coordinates of the point representing the qubit's state on the sphere's surface. These angles are directly related to the angles used in rotation gates in quantum circuits. Fig. 2 shows a qubit represented as a point on the Bloch sphere.
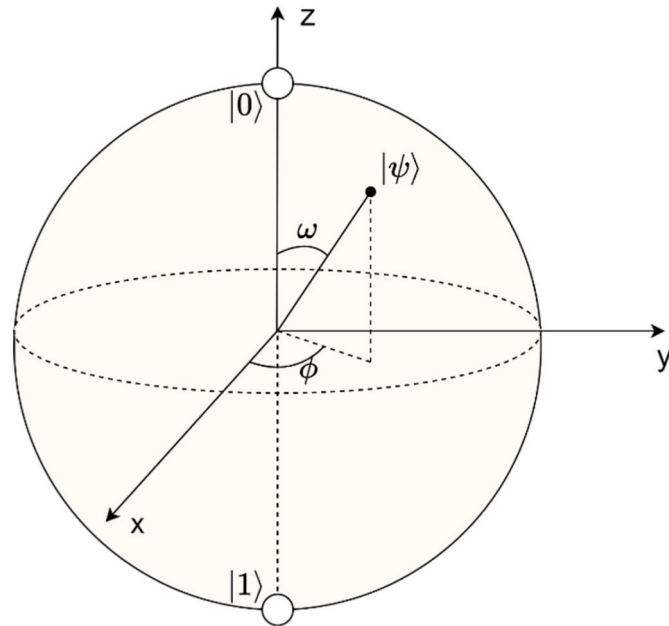

Fig. 2. A qubit represented as a point on the Bloch sphere, where ω is the angle from positive z-axis and parameter ϕ, an angle from positive x-axis. $|0\rangle$ represents a point on the north pole (positive z-axis) and $|1\rangle$ represents a point on the south pole (negative z-axis).

2.2.3. Entanglement

Entanglement is a fundamental phenomenon in quantum mechanics (Nielsen and Chuang, 2010) where two or more qubits become linked together in such a way that their states are intertwined, regardless of the distance separating them. A 2-qubit system is said to be entangled if it cannot be written as a tensor product of two individual qubit states. A common example of an entangled state is $a|00\rangle + b|11\rangle$. In this example, when a qubit is measured to be $|0\rangle$, we instantly know that another qubit is also $|0\rangle$, and similarly for $|1\rangle$. This strong correlation between measurements is a property of entanglement. Entanglement is a uniquely quantum mechanical phenomenon with no classical analog. The entanglement of a large number of qubits is infeasible to simulate on a classical computer; this makes quantum computing uniquely powerful. Entanglement is a vital ingredient in many quantum algorithms.

2.2.4. Quantum gates

Quantum gates are the fundamental building blocks of quantum circuits, analogous to logic gates in classical computing. They are unitary operations that act on one or more qubits, manipulating their quantum states. By combining different quantum gates in a specific way, quantum circuits are created which perform complex quantum algorithms. The commonly used quantum gates in the quantum circuits are rotation gates and Controlled-NOT (CNOT) gates. Rotation gates (Nielsen and Chuang, 2010) are a special class of single qubit gates that perform rotations of a qubit's state around a specific axis on the Bloch sphere. They are parameterized by angle θ. A general rotation gate $R_\nu(\theta)$ rotates the qubit's state around an arbitrary axis $\nu = (\nu_x, \nu_y, \nu_z)$ on the Bloch's sphere by an angle θ. For example, $R_x(\theta)$ rotates qubit's state around x-axis on the Bloch's sphere. The Hadamard gate is a special rotation gate that creates an equal superposition of the $|0\rangle$ and $|1\rangle$ states when applied to a computational basis state. It's usually used to generate superposition in quantum circuits.

The CNOT gate (Nielsen and Chuang, 2010) is a fundamental 2-qubit gate that is used to create entanglement between qubits. It operates on a controlled qubit and a target qubit. If the control qubit is in the state $|0\rangle$, the target qubit remains unchanged, but if the control qubit is in the state $|1\rangle$, the target qubit's state is flipped. When the control qubit is in a superposition state, the CNOT gate creates an entanglement between the control qubit and target qubit.

2.3. Model architectures

In this paper, we performed simulations using a classical LSTM model, a VQC, and two different types of quantum-classical hybrid models: one with a classical LSTM followed by a VQC, and another with a QLSTM, where the LSTM part of the model is created using VQCs.

2.3.1. Classical LSTM

A single-layer classical LSTM model with 128 hidden units was created for the comparison. LSTM is a type of RNN model. RNNs constitute a model family that processes data sequentially while preserving a hidden state. This hidden state is modified for every input in the sequence. During training, it learns to update the hidden state optimally, so that it can predict the next value in the sequence. LSTM is an RNN featuring complex memory cells and gate units for representing and updating memory. Each cell within an LSTM has three gates: a forget gate, an input gate and an output gate. At each time step t, the cell gets the current data point X_t along with the hidden state vector from the preceding time step h_{t-1} and the cell state vector from the preceding time step C_{t-1}. The forget gate determines which information to remove from the cell state. It accepts h_{t-1} and $X_{1:L}^t$ as inputs and processes them through a *sigmoid* function to generate values between 0 and 1 (Hochreiter, 1997). A value of 1 signifies complete retention, while 0 indicates complete forgetting. Mathematically,

$$f_t = \sigma_{forget}\left(W_f \cdot \left[h_{t-1}, X_{1:L}^t\right] + b_f\right) \qquad \text{(Equation 4)}$$

Here W_f and b_f represent the weight matrix and bias vector associated with the forget gate. The input gate determines which values will be updated. The candidate node (*tanh*) generates a vector of new candidate values that could be added to the state. The input gate employs a second *sigmoid* function to determine which state values to update, and a tanh function to generate a candidate vector of new values.

$$i_t = \sigma_{input}\left(\boldsymbol{W}_i \cdot \left[\boldsymbol{h}_{t-1}, \boldsymbol{X}_{1:L}^t\right] + \boldsymbol{b}_i\right) \qquad \text{(Equation 5)}$$

$$\widetilde{\boldsymbol{C}}_t = \boldsymbol{tanh}\left(\boldsymbol{W}_c \cdot \left[\boldsymbol{h}_{t-1}, \boldsymbol{X}_{1:L}^t\right] + \boldsymbol{b}_c\right) \qquad \text{(Equation 6)}$$

Here, W_i and b_i are the weight matrix and bias vector for the input gate. $\widetilde{C}_t$ is the candidate cell state vector, W_c and b_c are the weight matrix and bias vector associated with it. The cell state is updated by forgetting the old information (by multiplying the old cell state C_{t-1} by the forget gate's output) and adding the new candidate values.

$$C_t = \boldsymbol{f}_t \cdot \boldsymbol{C}_{t-1} + \boldsymbol{i}_t \cdot \widetilde{\boldsymbol{C}}_t \qquad \text{(Equation 7)}$$

The output gate determines which part of the cell states to output. It employs a *sigmoid* function to decide which parts of the cell state C_t to output, then processes the cell state through a tanh function and multiplies it with the output of the sigmoid function to generate the output hidden state h_t.

$$\boldsymbol{o}_t = \sigma_{output}\left(\boldsymbol{W}_o \cdot \left[\boldsymbol{h}_{t-1}, \boldsymbol{X}_{1:L}^t\right] + \boldsymbol{b}_o\right) \qquad \text{(Equation 8)}$$

$$\boldsymbol{h}_t = \boldsymbol{o}_t \cdot \boldsymbol{tanh}(\boldsymbol{C}_t) \qquad \text{(Equation 9)}$$

The LSTM layer of the model is followed by a fully connected layer that transforms its output into the final output. Mean Squared Error (MSE) is used to calculate the loss, and Adam optimization (Kingma, 2014) approach is used as an optimizer to update the weights. Fig. 3 shows the schematic diagram of a classical LSTM model with an LSTM cell expanded to show gates.

2.3.2. Variational Quantum Circuit

VQCs are quantum algorithms that are used to build quantum machine learning models (Chen et al., 2020). Both the hybrid quantum-classical LSTM and QLSTM are built using VQCs. VQC mainly consists of three parts. The first part is used to transform the input classical information into quantum information. This is done by encoding the input information as rotation angles in rotation gates like the Rotation-Y (RY) gate, which rotates a fixed qubit $|0\rangle$ around the Y-axis based on the input. The second part is a quantum circuit

composed of rotation gates and CNOT gates. The rotation gates have free parameters $\theta = (\theta_1, \theta_2, \ldots)$ as the rotation angles. These parameters can be tuned using classical algorithms like gradient descent to optimize a cost function. The CNOT gates are used to entangle the qubits. The final part is the measurement unit, which is used to turn back quantum information to classical information by evaluating the expectation value. Fig. 4 shows a 4 qubit VQC along with classical input and output MLP layers. It uses RY rotation to transform input classical information into quantum information. The parameterized circuit consists of a rotation gate on each wire, with CNOT gates connecting pairs of wires, resulting in entanglement between qubits. Finally, the Pauli-Z operator is used for measuring expectation value.

2.3.3. Hybrid quantum-classical LSTM

The hybrid quantum-classical LSTM consists of a classical LSTM layer, an intermediate fully connected layer, a VQC, and a final fully connected layer. The sequence data is fed as input to the classical LSTM layer, the output of which is passed to a fully connected layer to map to a representation with a shape equal to the number of qubits in the VQC. Within the VQC, rotation gates are used to encode classical data into quantum information. The VQC contains three parameterized rotation gates in sequence, as shown in Fig. 4, to process the quantum information. The output of the VQC is the expectation value measured with the Pauli-Z operator. This output is then fed into a final fully connected layer, which outputs the next value in the sequence. We used MSE as the loss function and the Adam optimizer to update the weights.

2.3.4. QLSTM

The principle behind QLSTM (Chen et al., 2022) is the same as the classical LSTM. It contains a similar sequence of operations and analogous gates, where the core computations for determining gate values are replaced by quantum operations. Specifically, the matrices serving as parameters in a classical LSTM are replaced by parameterized quantum circuits (VQCs) with rotation angles as their tunable parameters. Equations (10)–(15) represent the QLSTM cell's computations, showing how VQCs generate gate activations that, through LSTM-like update rules using classical activation functions ($\sigma, tanh$) and arithmetic, modify the cell state (C_t) and hidden state (h_t) based on previous states.

$$\boldsymbol{f}_t = \sigma_{forget}\left(\boldsymbol{VQC}_1\left(\left[\boldsymbol{h}_{t-1}, \boldsymbol{X}_{1:L}^t\right]\right)\right) \qquad \text{(Equation 10)}$$

$$\boldsymbol{i}_t = \sigma_{input}\left(VQC_2\left(\left[h_{t-1}, X_{1:L}^t\right]\right)\right) \qquad \text{(Equation 11)}$$
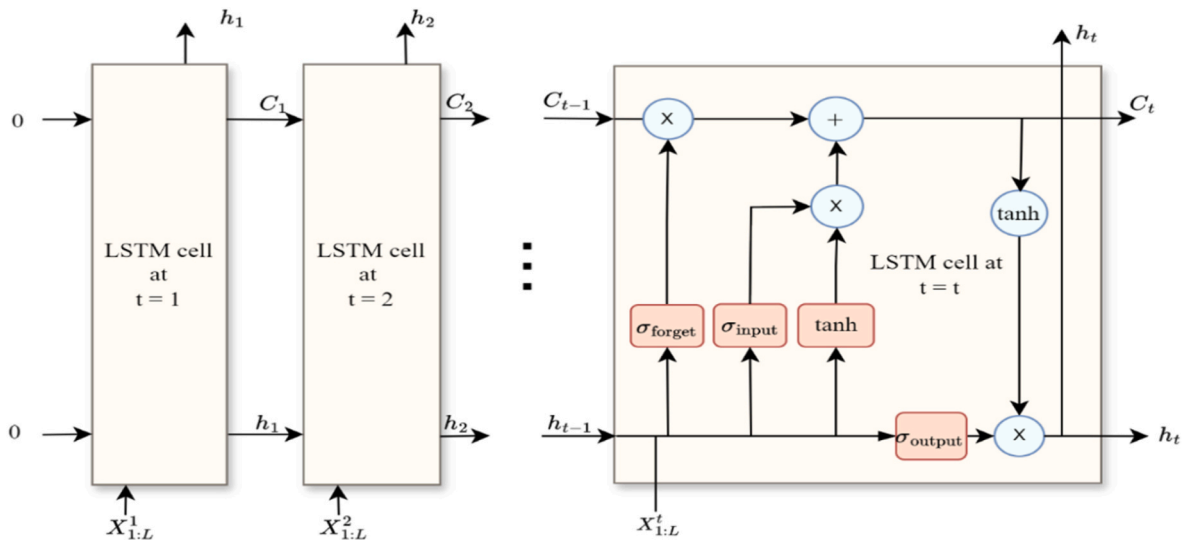

Fig. 3. Schematic diagram of a classical LSTM model. C_t represents the cell state at time step t, h_t represents the hidden state at time step t, X^t represents the input to LSTM model at time step t and σ represents gates in a LSTM cell.

Classical Operations   **Quantum Operations**   **Classical Operations**
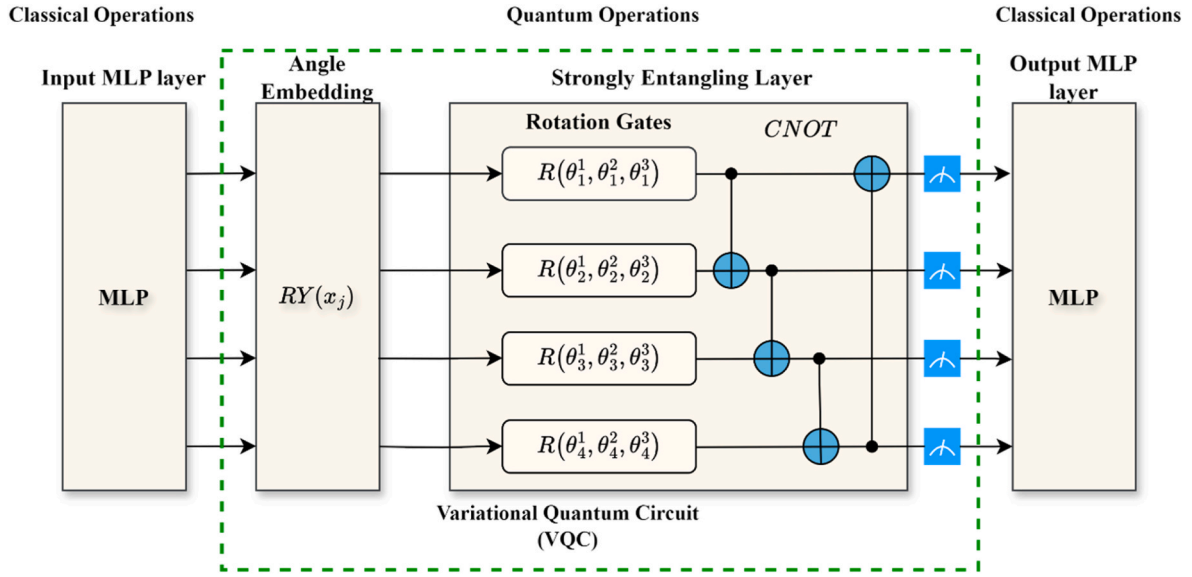

Fig. 4. The workflow of VQC with input and output multilayer perceptron layers. x_j refers to the inputs to the angle embedding layer which embeds the input into rotation angles. The rotation angles are passed to the parameterized quantum circuit. R represents rotation gates and θ refers to the trainable parameters in VQC. It depicts a single-layer VQC with four qubits.

$$\widetilde{C}_t = \tan h\big(VQC_3\big(\big[h_{t-1}, X_{1:L}^t\big]\big)\big) \qquad \text{(Equation 12)}$$

$$C_t = f_t \cdot C_{t-1} + i_t \cdot \widetilde{C}_t \qquad \text{(Equation 13)}$$

$$o_t = \sigma_{output}\big(VQC_4\big(\big[h_{t-1}, X_{1:L}^t\big]\big)\big) \qquad \text{(Equation 14)}$$

$$h_t = o_t \cdot \tan h(C_t) \qquad \text{(Equation 15)}$$

We used 4 qubit VQCs to build the QLSTM. The given feature vector was first mapped to a latent space with dimensions equal to the number of qubits using a fully connected layer. Then, this output was used as input to the QLSTM model. The output of the QLSTM was again mapped to the required shape (in our case next value in the sequence) using another fully connected layer. MSE was used as the loss function, and the Adam optimizer was used to optimize training parameters. Fig. 5 shows the workflow of QLSTM.

2.4. Evaluation metrics

In this study, we adopted three distinct metrics, Nash-Sutcliffe Efficiency (NSE), Kling-Gupta Efficiency (KGE), and Mean Absolute Error (MAE), to comprehensively evaluate model performance. Rather than

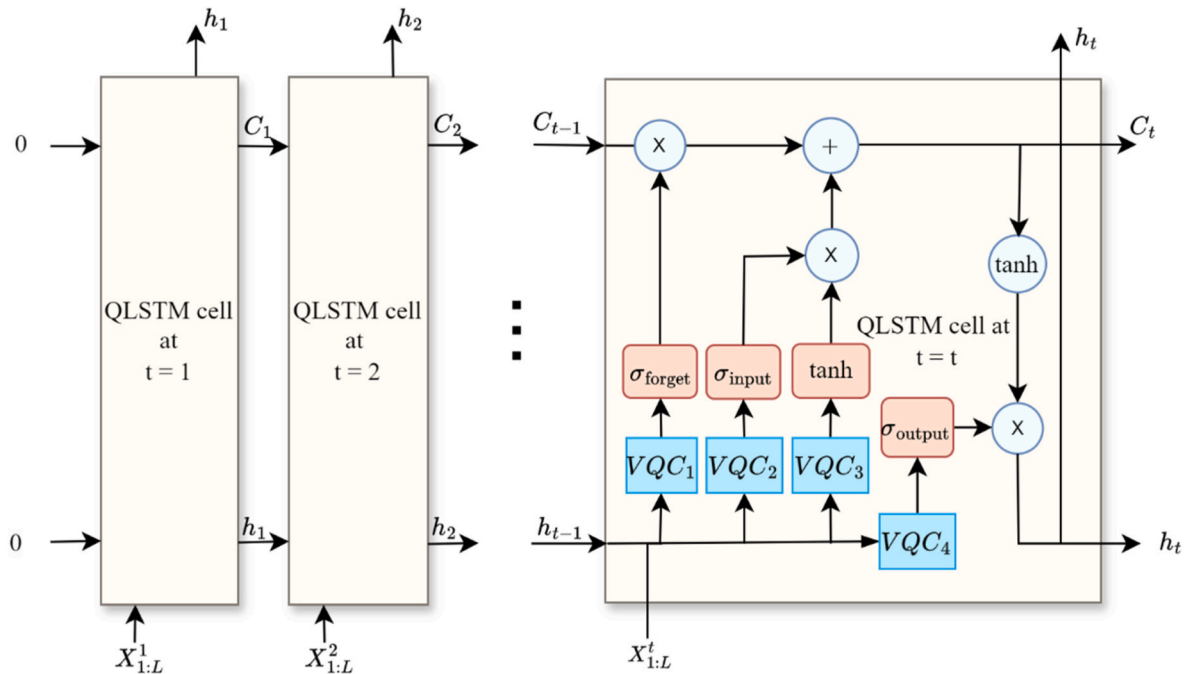**Fig. 5.** Schematic diagram of QLSTM. C_t represents the cell state at time step t, h_t represents the hidden state at time step t, X^t represents the input to LSTM model at time step t and σ represents gates in a LSTM cell. Here, VQCs are used to implement the gates. Note that the intermediate values are embedded into angles by classical computers before passing them to the quantum circuits.

focusing solely on a single dimension of error, these metrics collectively capture agreement in flow patterns, consistency in statistical properties, and the magnitude of deviations.

The NSE serves as a diagnostic of how well the model captures the temporal variability of streamflow. This metric is based on comparing the squared differences between model outputs and observations against the variance of the observed data. An NSE score of 1 indicates perfect agreement, while a value of 0 suggests that the model performs no better than using the mean of the observations. Negative values indicate that the model introduces more error than a constant-mean prediction. The mathematical expression for NSE is:

$$NSE = 1 - \frac{\sum_{i=1}^{n} \left(Q_{s_i} - Q_{o_i}\right)^2}{\sum_{i=1}^{n} \left(Q_{o_i} - \overline{Q_o}\right)^2} \qquad \text{(Equation 16)}$$

where Q_{o_i} and Q_{s_i} represent the observed and simulated streamflow at time i, $\overline{Q_o}$ denotes the mean observed flow, and n is the number of data points considered.

Beyond assessing variance reproduction, model evaluation also benefits from accounting for correlation and scaling errors, where KGE becomes particularly important. KGE decomposes model performance into three components: correlation strength, bias in the mean, and variability in error. It then synthesizes these components into a single score. The KGE formulation reduces the likelihood that a model achieves a high score due to compensating errors. The KGE metric is defined as:

$$KGE = 1 - \sqrt{(r - 1)^2 + (\alpha - 1)^2 + (\beta - 1)^2} \qquad \text{(Equation 17)}$$

Here, r stands for the Pearson correlation coefficient, α is the ratio of the simulated to observed means ($\alpha = \frac{\mu_s}{\mu_o}$), and β measures the relative variability ($\beta = \left(\sigma_s/\mu_s\right)/\left(\sigma_o/\mu_o\right)$), with μ and σ representing the mean and standard deviation, respectively.

Finally, MAE was included to provide an intuitive and direct evaluation of simulation accuracy. NSE and KGE are sensitive to large errors due to their reliance on squared terms, whereas MAE treats all deviations equally by taking the average of absolute differences. It reflects the typical magnitude of simulation errors without disproportionately weighing outliers:

$$MAE = \frac{1}{n} \sum_{i=1}^{n} \left|Q_{o_i} - Q_{s_i}\right| \qquad \text{(Equation 18)}$$

where Q_{o_i} and Q_{s_i} are the observed and simulated values, respectively, at each time step i.

2.5. Experimental setup

The overall workflow of our research is illustrated in Fig. 6. The CAMELS dataset contains streamflow data from USGS stations, complemented by Daymet-derived meteorological forcing data. Water quality data was obtained from USGS stations and supplemented with NLDAS-derived meteorological forcing data. The dataset was then processed through a rigorous pipeline including data filtering, missing value imputation, and standardization. We performed time series simulations for both datasets and conducted sensitivity analysis and generalization analysis for streamflow data only. To quantify the importance of each meteorological predictor, we performed a leave-one-variable-out sensitivity analysis following the approach of Pianosi and Wagener (2015) for daily streamflow. For each zone and station, we first trained a baseline model using all six meteorological forcings, while keeping the model settings identical across experiments. We then repeated training from scratch six times, each time excluding exactly one predictor.

For each station we computed NSE on the held-out test period and defined the NSE drop attributable as:

$$\Delta NSE = NSE_{all} - NSE_{without\ variable} \qquad \text{(Equation 19)}$$

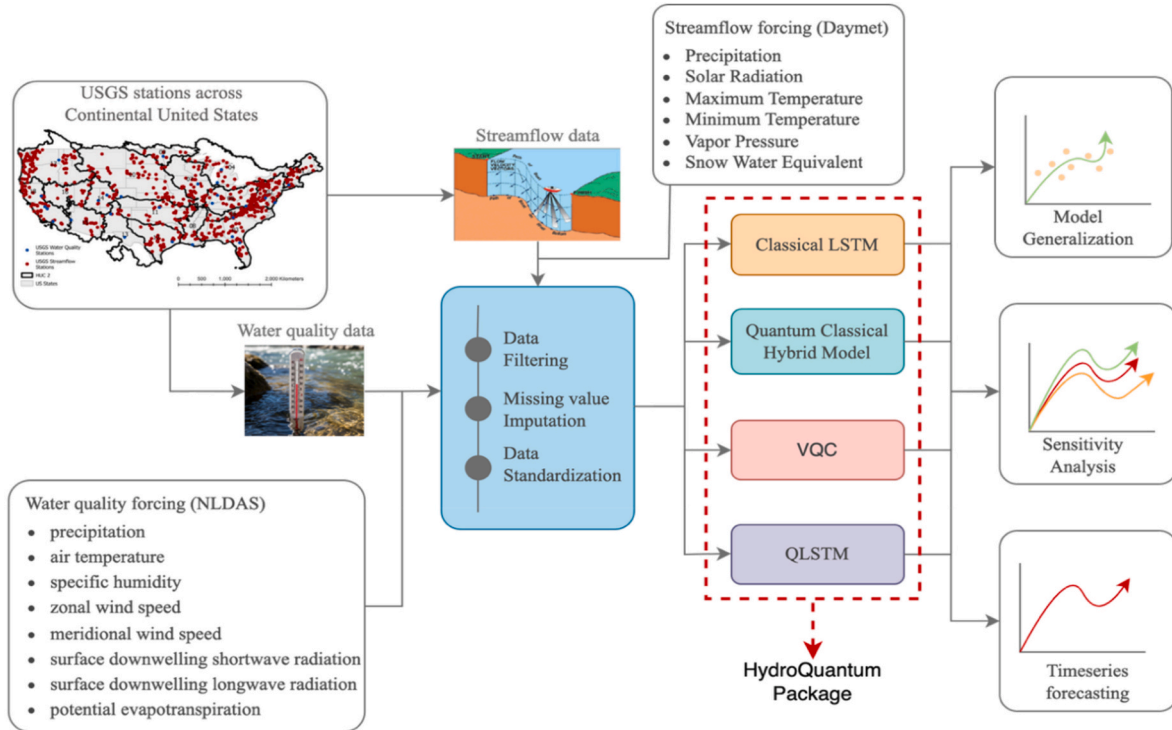where NSE_{all} denotes the baseline performance using all input variables

Fig. 6. The workflow of HydroQuantum includes creating three different quantum-driven algorithms for daily streamflow and water quality simulation across CONUS.

and NSE$_{without\ variable}$ represents the performance when a specific predictor was omitted. After computing ΔNSE for each station, results were then averaged within each zone to obtain zone-level sensitivity values.

Generalization analysis involved selecting multiple stations from each zone, training on a subset, and testing on the remaining unseen stations. The purpose of the sensitivity and generalization analyses was to evaluate the capability of the QLSTM model; therefore, the analysis was limited to the CAMELS dataset, which exhibited greater variability in results. All these approaches were assembled and packaged as "HydroQuantum".

The classical LSTM was implemented using PyTorch (Paszke et al., 2019), whereas the quantum circuits and computations were simulated using Pennylane (Bergholm et al., 2018). Experiments were conducted on Clemson University's high-performance computing Palmetto cluster. We trained each model separately for each station and collected the results. The models were trained and evaluated in parallel across different nodes, each with one high-performance Intel CPU core and 8 GB of RAM. Each model was trained with a batch size of 64 for 140 epochs. All experiments were conducted with a lookback window of 30 days with simulations for the next day.

3. Results and discussion

3.1. Performance assessment

Table 1 and Fig. 7 present the predictive skill of QLSTM, VQC, the classical LSTM, and a hybrid quantum-classical LSTM for 18 zones or HUC2. Across all zones, QLSTM yielded the highest mean NSE (0.60), indicating suggesting improved of daily streamflow data, whereas the classical LSTM achieved the lowest mean MAE (103.9 m³ s⁻¹). The hybrid quantum-classical LSTM attained the highest mean KGE (0.65), revealing the best overall balance of correlation, bias, and variability. VQC achieved a mean NSE of 0.49, a mean MAE of 107.3 m³ s⁻¹, and a mean KGE of 0.62, indicating moderate performance across metrics with strengths in specific zones. These findings highlight the complementary strengths of each model architecture and suggest that the choice of the model may depend on specific objectives, such as bias in data, error magnitude, and hydrological variabilities. However, given that NSE directly reflects a model's ability to reproduce the dynamics of streamflow over time, the comparatively higher NSE performance of QLSTM underscores its value as the most robust and informative metric compared to the classical LSTM, VQC, and the hybrid quantum-classical LSTM.

Individual zone simulation revealed a strong correlation between daily streamflow simulations and the prevailing hydroclimatic conditions in different regions. Snow- and rainfall-dominated basins such as the Souris-Red-Rainy, Upper Colorado, and Great Basin regions (zones 9, 14, and 16) showed higher performance for all models (NSE ≥0.93, KGE ≥0.87); nonetheless, the hybrid quantum-classical LSTM consistently delivered the lowest MAE and the highest KGE. In contrast, urbanized or flashy basins in zones 2, 5, 7, and 11 showed significant decline in NSE (0.34–0.53) values for all models. Here, QLSTM retained a modest improvement in NSE due to its quantum-inspired gating that captures peak flow variability well. When considering overall performance across all zones, the classical LSTM achieved the lowest mean MAE (103.9 m³ s⁻¹), indicating its effectiveness in minimizing absolute error. While the classical LSTM achieves the best average MAE across all zones (103.9 m³ s⁻¹), the optimal model for minimizing absolute error varies regionally. The QLSTM yielded the lowest MAE in Zones 1, 6, 8, 9, 10, and 13, whereas the hybrid quantum-classical LSTM was superior in Zones 3, 4, 12, 14, 15, and 16. The classical LSTM led only in Zones 7 and 18, and the VQC was occasionally optimal in rapid-response catchments like Zone 11. This variability underscores that MAE, which is sensitive to the flow magnitude characteristic of each basin, is an insufficient metric for ranking model performance across diverse hydrological regimes.

3.2. Daily streamflow simulation

We used the first ten years (October 1, 2000, to October 1, 2010) of daily streamflow data for training and validation while the subsequent four years (October 2, 2010, to September 30, 2014) were used for testing. Simulation results revealed that basins prone to extreme tropical cyclones, such as those located in the Texas–Gulf and Lower Colorado regions (zones 12 and 15), presented unique challenges for quantum-driven models. Both QLSTM and classical LSTM returned negative NSE and KGE values, whereas the hybrid quantum-classical LSTM showed improved NSE of 0.24. VQC also struggled in these zones with negative NSE (e.g., NSE of −2.29 in zone 12) and low KGE (e.g., KGE of −0.02 in zone 12), indicating limited ability to handle extreme events. In contrast, large, regulated river systems like the Lower Mississippi, Missouri, and Rio Grande (zones 8, 10, and 13) exhibited distinct performance patterns. For example, Zone 13 (Rio Grande region) demonstrated strong performance across all models, with the hybrid quantum-classical LSTM achieving the highest KGE (0.85), followed closely by VQC (0.82) and QLSTM (0.81).

In addition, the VQC performance was generally competitive in

Table 1
Comparative performance of QLSTM, classical LSTM, hybrid quantum-classical LSTM, and VQC across 18 zones, using three standard evaluation metrics: MAE, NSE, and KGE. The bottom row reports the average performance across all zones. The best performance in each zone is shown in bold.

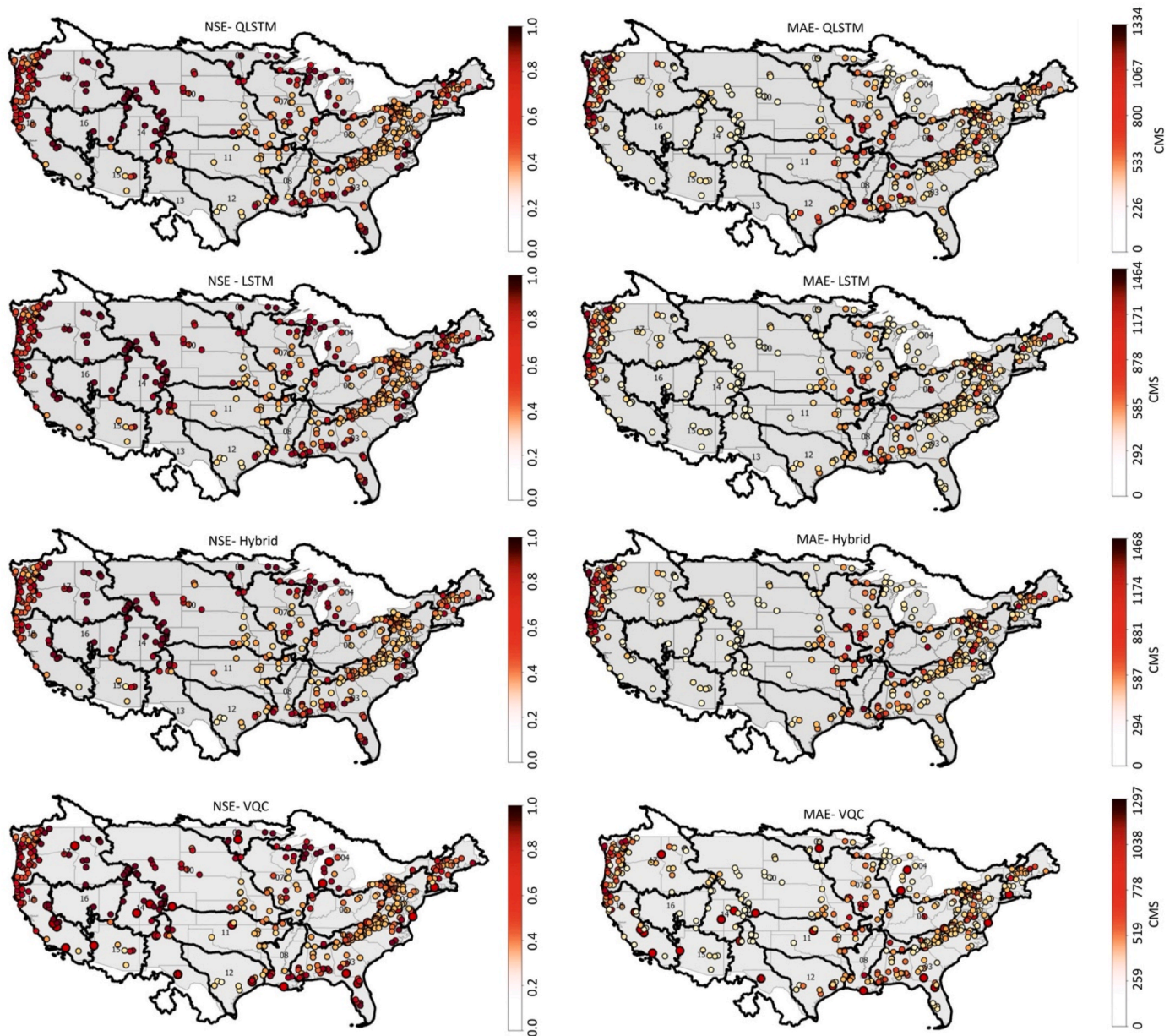| Zone	MAE				NSE				KGE			
	QLSTM	LSTM	Hybrid	VQC	QLSTM	LSTM	Hybrid	VQC	QLSTM	LSTM	Hybrid	VQC
1	**107.16**	121.9	124.2	108.2	**0.59**	0.56	0.55	0.58	0.64	0.65	**0.66**	0.64
2	90.74	93.15	96.2	**87.22**	**0.44**	0.43	0.43	0.42	0.48	0.48	**0.51**	0.47
3	82.79	82.59	**81.58**	97.93	**0.56**	0.51	0.5	0.53	0.58	0.58	**0.6**	0.52
4	59.2	59.08	**57.31**	58.83	**0.78**	0.77	0.76	0.76	0.79	0.78	**0.81**	0.78
5	110.8	101.3	112.7	**99.74**	**0.53**	0.49	0.51	0.51	0.58	**0.61**	**0.61**	0.58
6	**106.84**	117.4	107.7	123.3	**0.56**	0.5	0.49	0.54	**0.61**	0.57	**0.61**	0.59
7	160.72	**138.1**	149.2	179.6	**0.52**	0.46	0.44	0.48	0.49	**0.58**	0.58	0.45
8	**232.95**	240.3	238	240	**0.64**	0.59	0.61	0.63	0.61	**0.65**	0.64	0.64
9	**51.28**	60.53	53.19	62.97	**0.96**	**0.96**	0.95	0.95	0.92	0.9	0.92	**0.94**
10	**47.72**	54.1	57.79	60.69	**0.68**	0.64	0.62	0.65	0.62	0.62	**0.63**	0.59
11	97.33	82.47	93.57	**77.30**	0.37	0.35	0.34	**0.39**	0.12	0.3	0.24	**0.40**
12	121.4	74.44	**65.5**	76.17	−0.04	−0.01	**0.24**	−2.29	−0.9	−0.48	−0.09	**−0.02**
13	**3.68**	4.38	3.7	3.75	**0.82**	0.79	0.81	0.80	0.81	0.77	**0.85**	0.82
14	6.63	6.57	**5.96**	8.46	**0.98**	0.97	**0.98**	0.97	0.93	0.94	**0.95**	0.93
15	21.67	13.4	**12.53**	14.25	0.29	**0.42**	0.37	0.39	−0.03	0.38	**0.53**	0.31
16	4.05	3.36	**3.13**	3.27	0.93	**0.94**	0.93	**0.94**	0.87	0.91	**0.95**	0.93
17	178.24	172.2	174.3	**168.9**	**0.78**	0.74	0.74	0.76	0.81	0.81	**0.82**	**0.82**
18	210.5	**179.8**	184.4	183.1	0.7	**0.73**	0.71	**0.73**	0.72	0.76	**0.78**	**0.78**
Average	107.71	**103.9**	105.7	107.3	**0.6**	0.57	0.55	0.49	0.6	0.62	**0.65**	0.62

Fig. 7. Comparison of NSE and MAE values for different models across different zones.

regulated river systems, achieving NSE values of 0.63–0.80 and KGE values of 0.59–0.82 in zones 8, 10, and 13. However, compared to QLSTM, VQC fell short in consistently capturing temporal variability in data. Overall, VQC showed comparable MAE to QLSTM in zones 2 and 11 only, where the HUC is dominated by urbanization.

Fig. 8 presents the simulation results for four selected gauging stations. As illustrated, at Oyster River (zone 1; see Fig. 8a), all models achieved comparable NSE values (~0.66–0.73) and relatively low MAEs. The hybrid quantum-classical LSTM yielded the lowest MAE (6.77 m³/s) and highest KGE (0.81), suggesting slightly improved consistency in simulation compared to QLSTM and classical LSTM. At Manatee River (zone 3; see Fig. 8b), the classical LSTM achieved the lowest MAE (37.91 m³/s), while QLSTM slightly outperformed the other models in terms of NSE (0.78). Meanwhile, the hybrid quantum-classical LSTM produced the highest KGE (0.81), demonstrating robustness in capturing daily streamflow patterns despite having a higher MAE. Paint Rock River, located in zone 6 (see Fig. 8c), is characterized by notably higher flow variability. In this basin, QLSTM showed the lowest MAE and the highest NSE (0.86), highlighting the strength of this algorithm in

predicting peak flow values. At Bad River, located in zone 4 (see Fig. 8d), all models performed well, achieving high NSE values (≥0.85) and relatively low MAEs. The hybrid quantum-classical LSTM exhibited the best overall performance with the lowest MAE (178.94 m³/s) and highest KGE (0.92), indicating strong agreement with observations.

3.3. Cumulative distribution functions (CDFs)

Figs. 9 and 10 present the CDF plots of NSE and MAE, respectively, for all modeling configurations. These CDFs illustrate the distribution of model performance across all catchments within each of the 18 zones across CONUS. As illustrated, in nearly all zones, the QLSTM model exhibited superior performance compared to the classical LSTM, the VQC, and the hybrid quantum-classical LSTM. As shown, the CDF curve of QLSTM is positioned furthest to the right, indicating a higher NSE performance across CONUS. Furthermore, the CDF curve of the MAE values for QLSTM shifted further to the left, signifying a lower simulation error for most basins compared to the other models. Notable exceptions observed in zones 11, 12, 15, 16, and 18, where QLSTM
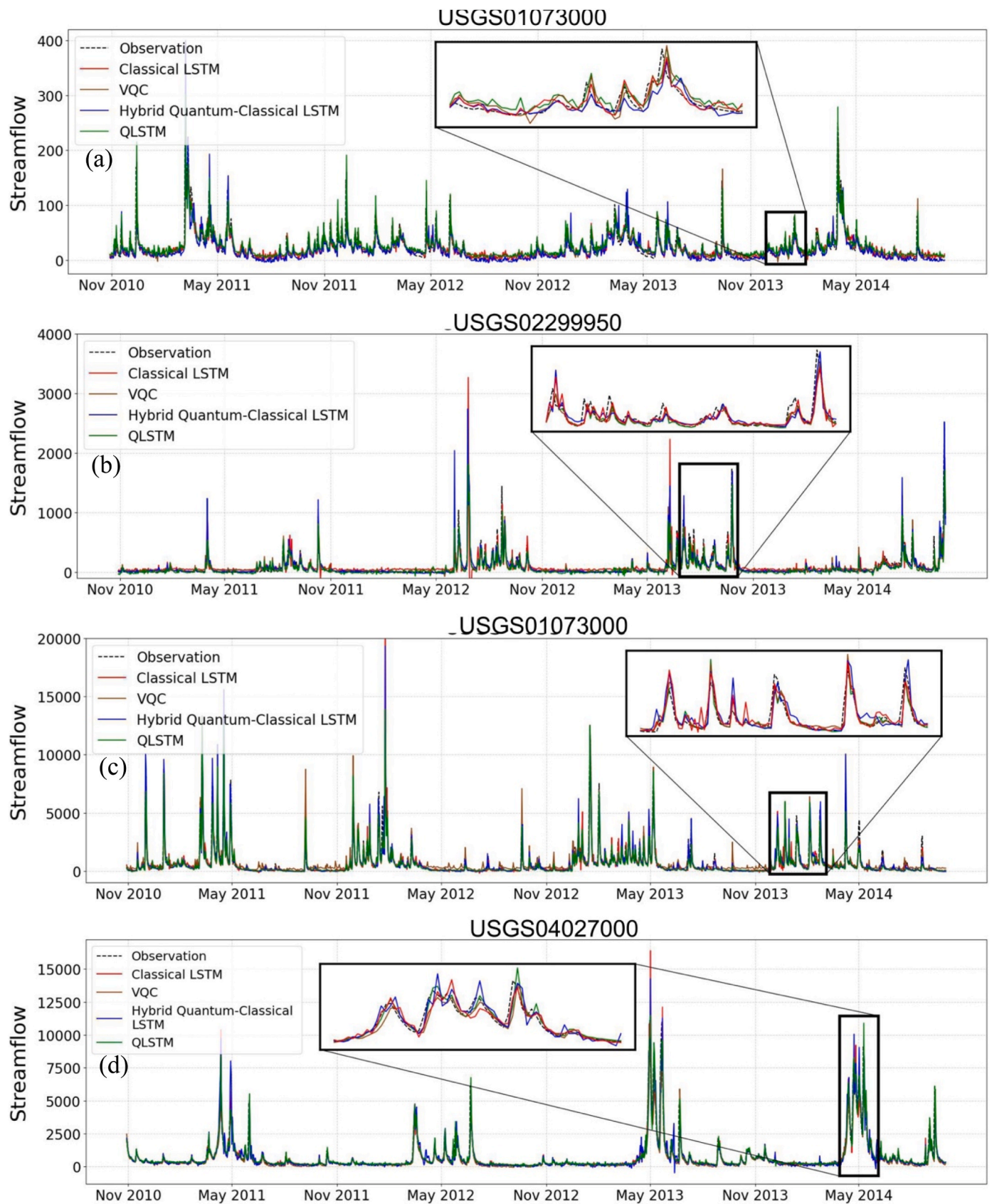
Fig. 8. Streamflow simulation results at four selected USGS gauging stations: (a) 01073000, (b) 02299950, (c) 03574500, and (d) 04027000. Each panel compares observed streamflow (black dashed line) with outputs from the models: Classical LSTM (red), VQC (orange), hybrid quantum-classical LSTM (blue), and QLSTM (green). Each subplot zooms in on a representative high-flow period to highlight the ability of models to capture peak flow dynamics and temporal variability in data. (For interpretation of the references to colour in this figure legend, the reader is referred to the Web version of this article.)
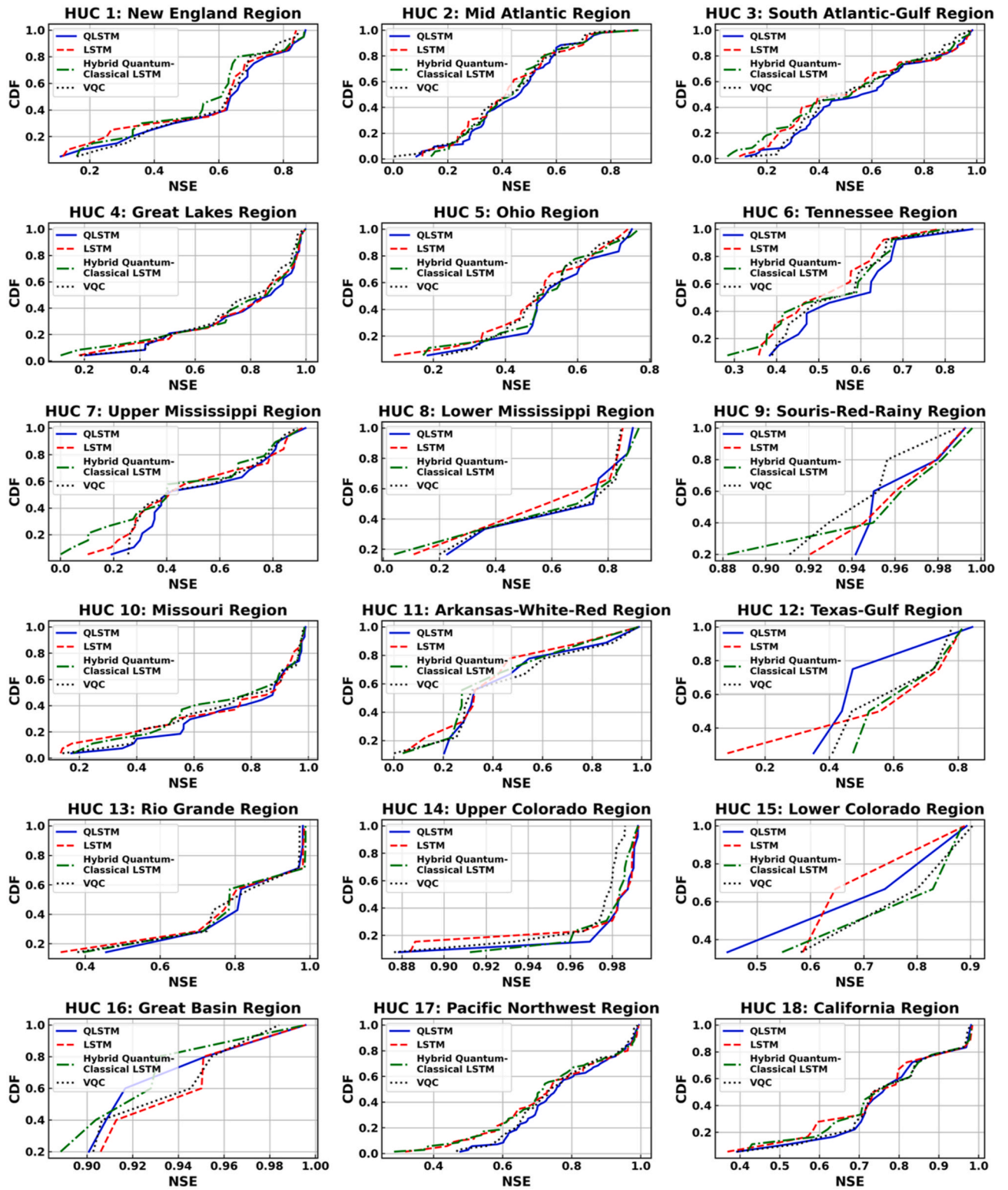
Fig. 9. The CDF curves of NSE values for the model configurations across 18 zones. For each zone and each model, station-level NSE scores (filtered to include only non-negative values) were sorted in ascending order, and then CDF curves were created, where each NSE value represents the fraction of stations with an NSE value that is less than or equal to it.

exhibited the least desirable performance. In addition, the relative performance between the classical LSTM, VQC, and the hybrid quantum-classical LSTM was region-dependent. For example, in zones 1, 8, 11, and 17, the VQC outperformed both the classical LSTM and the hybrid quantum-classical LSTM, achieving both a higher NSE and a lower MAE.

In contrast, the hybrid quantum-classical LSTM outperformed the other two models in zones 12 and 14, while the classical LSTM performed best in zones 15 and 16. In the remaining zones, each model excelled on one metric but not the other, indicating mixed performance. This suggests that the benefit of quantum augmentation varies with local hydrologic
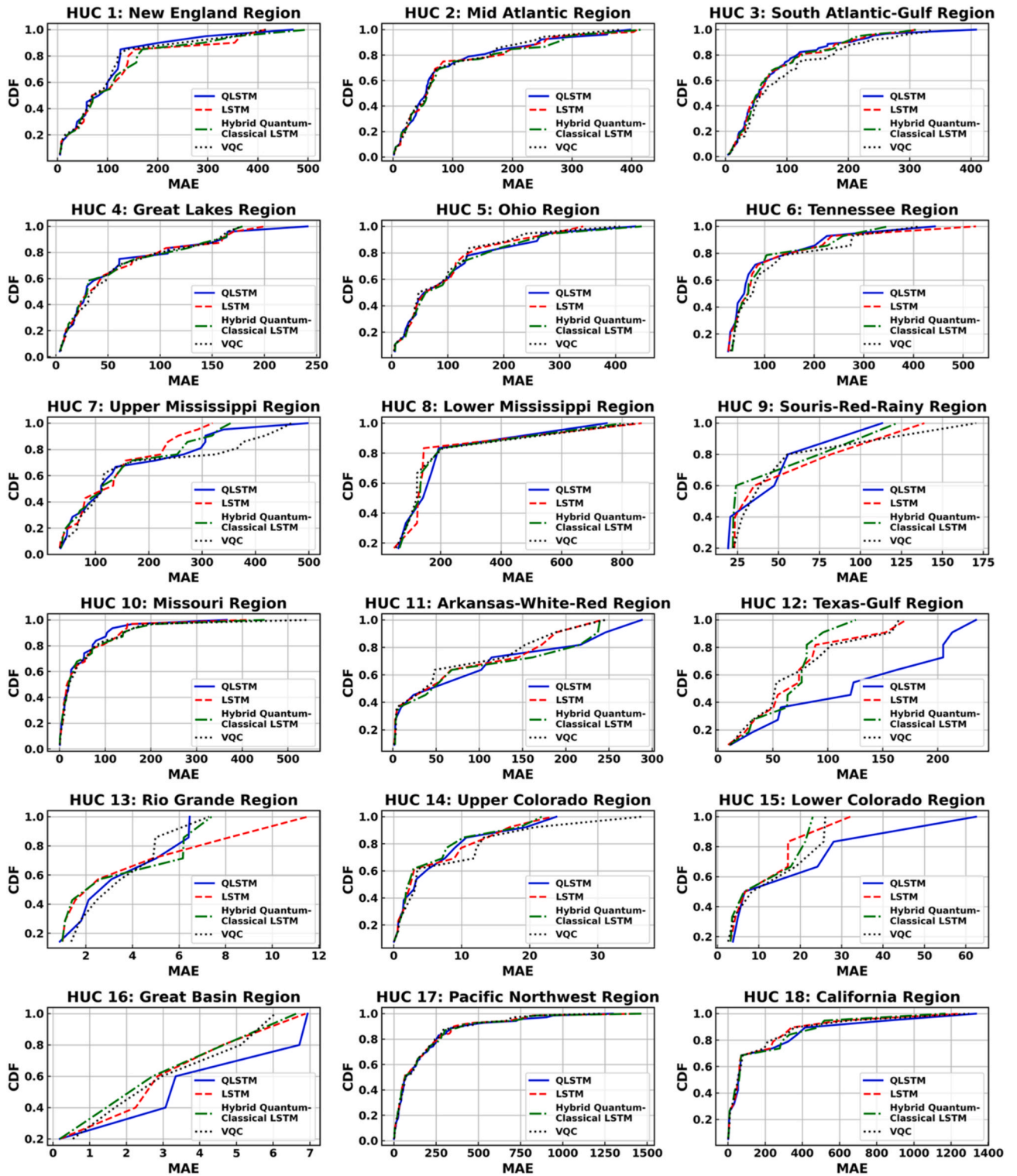
Fig. 10. The CDFs of MAE for all the models across 18 zones. For each zone and each model, station-level MAE scores were sorted in ascending order, and then CDF curves were created, where each MAE value represents the fraction of stations with an MAE value that is less than or equal to it.

conditions, rainfall variability, snowmelt-driven flow, and flow regulation.

In urbanized and flashy basins (zones 2, 5, and 7), QLSTM demonstrated more favorable NSE distributions than all other models, with over 60 % of stations achieving NSE ≤0.62 compared to up to 0.45 for the classical LSTM. The richer representational capacity introduced by quantum embedding allowed QLSTM to better capture short-lived, high-

magnitude runoff peaks generated by intense rainfall, which the other architectures often underfit. In large and partially regulated river systems (zones 10 and 13), QLSTM again outperformed the remaining models, achieving median NSE values above 0.80 and median MAE values below 25 m^3 s^{-1}. The smoother long-term flow signals arising from extensive drainage areas and moderate regulation aligned well with QLSTM's ability to capture extended dependencies while still

accommodating shorter variability. In rainfall-dominated regions such as zone 12, however, this advantage diminished: QLSTM lagged behind the hybrid quantum–classical LSTM, with median NSE values falling well below 0.5. This underperformance reflects the strong non-stationarity introduced by occasional tropical storms and coastal storm surges, which disrupt the persistence that QLSTM depends on. In zone 15, heavy reservoir regulation created abrupt discontinuities in the flow time series, such as sudden releases or sustained low flows. In this setting, both the classical LSTM and the hybrid quantum–classical LSTM occasionally outperformed QLSTM by better balancing short-term fluctuations with seasonal signals. In arid basins (zone 16), where streamflow magnitudes and MAE values were already very low (typically <10 $m^3 s^{-1}$), quantum augmentation provided little additional benefit, as all models achieved similar accuracy.

The NSE results, shown in Fig. 9, further revealed satisfactory performance for most zones. Regions with particularly strong performance included zone 9 (Souris-Red-Rainy Region), zone 13 (Rio Grande Region), zone 14 (Upper Colorado), zone 16 (Great Basin Region), and zone 17 (Pacific Northwest), all of which exhibited median NSE values above 0.80 across all configurations. Conversely, some zones consistently showed unsatisfactory performance across all models, with median NSE values below 0.5. These include zone 2 (Mid-Atlantic), zone 11 (Arkansas-White-Red), zone 12 (Texas-Gulf), and zone 15 (Lower Colorado Region). The sub-performance in zones 2 and 11 likely stems from erratic rainfall patterns and flashy runoff responses, which made it difficult for quantum-driven models to learn stable relationships. MAE results further revealed substantial regional variation, largely driven by climate and catchment variabilities (see Fig. 10). Arid and semi-arid regions with low streamflow values, such as zones 13 (Rio Grande) and 16 (Great Basin), exhibited very low MAE values (often $<10 \, m^3 s^{-1}$). In contrast, regions encompassing large river systems and higher precipitation amounts, like zones 17 (Pacific Northwest) and 18 (California), showed much larger MAE values, with errors reaching up to $\sim 1400 \, m^3 \, s^{-1}$ and median errors around $100 \, m^3 \, s^{-1}$. These western coastal basins (HUC-17 and HUC-18) are characterized by complex topography, pronounced seasonal variability, and intensive water management, all of which contribute to elevated simulation uncertainties.

The shape of the CDF curves further revealed important patterns in streamflow simulation and performance distribution within each zone. NSE performance is illustrated by a curve shifted far to the right with a steep slope, suggesting consistently high performance across most zones (see Fig. 9). For example, the CDFs of zones 4 and 14 rose sharply to high NSE thresholds (e.g., above 0.8), indicating that the majority of gauging stations in these zones performed well. In contrast, zones 2, 11, and 12 often displayed CDFs that were shifted significantly to the left with a gentle slope and prominent right tails, indicating that the majority of these regions exhibited unsatisfactory performance.

The CDF curves associated with MAE exhibited a steep initial rise followed by a long upper right tail (see Fig. 10). This implies that while the majority of catchments within a zone might have relatively low MAE, a subset of catchments experienced substantially higher errors, leading to significant instability in the models. For instance, in South Atlantic-Gulf (zone 3) the errors extended to over 400 m^3/s for the worst-performing catchments, highlighting significant intraregional performance variability.

3.4. Water quality analysis

In this study, daily SWT simulation was performed using classical LSTM, QLSTM, hybrid quantum-classical LSTM, and VQC for 27 USGS gauging stations across CONUS. The data for SWT, which serves as a proxy for water quality, were obtained directly from USGS databases, as the CAMELS dataset does not include SWT. To ensure robust evaluation, we selected stations that provided continuous data from October 1, 2015, to September 30, 2022, with fewer than 30 consecutive days of

missing values. Meteorological forcings were derived from the NLDAS dataset, including precipitation, air temperature, humidity, horizontal wind components, downward shortwave and longwave radiation, and potential evaporation. The models were trained and validated from October 1, 2015, to September 30, 2020, and tested from October 1, 2020, to September 30, 2022. The performance of all models was evaluated for each USGS gauging station (see Table 2).

As shown in Table 2, overall, the classical LSTM slightly outperformed the other models for SWT, yielding the lowest errors on average across the 27 stations. The hybrid quantum–classical LSTM ranked second, while QLSTM and VQC performed slightly lower. Inspection of individual station results (Table 2 and Fig. 11) reveals important insights. While the classical LSTM consistently produced the lowest MAE values across most stations, the hybrid quantum-classical LSTM achieved superior KGE values in many stations. This highlights the fact that the hybrid quantum-classical LSTM captured the overall structure of SWT dynamics well, including seasonal variability and long-term fluctuations. Although the QLSTM model slightly lagged in terms of MAE, it still provided robust simulation with NSE values exceeding 0.95 at most stations. Notably, QLSTM outperformed both the hybrid quantum-classical LSTM and classical LSTM in several stations such as Pecos River at Red Bluff, NM (USGS-08407500), West Clear Creek near Camp Verde, AZ (USGS-09505800), and Walker River near Wabuska, NV (USGS-10301500). This algorithm surpassed the other models in these stations where dependencies within SWT data changed over time. VQC simulation suggested that this standalone quantum approach demonstrated competitive performance with mean NSE values of 0.982 across all stations, achieving the highest KGE scores at 11 out of 27 stations including Colorado River at Lees Ferry, AZ (USGS-9380000) and Pecos River at Red Bluff, NM (USGS-08407500). However, the VQC approach showed slightly higher MAE values compared to classical methods, indicating some challenges in minimizing absolute prediction errors despite its strong correlation performance.

Since SWT generally has a regular and less complex trend than streamflow data, all models achieved superior performance across different zones. In this context, the classical LSTM proved to be particularly well-suited due to its relatively simple architecture and effective memory mechanisms. More importantly, classical LSTM was more efficient in learning patterns and seasonal trends in data without the added complexity of quantum components. In contrast, the inclusion of VQC component to QLSTM and the hybrid quantum-classical LSTM provided no differences in performance results, reflecting the fact that SWT data posed no unique challenges for the models. This analysis further revealed that classical LSTM is well suited for SWT simulation since the algorithm can retain information over extended periods, allowing the model to capture and learn from recurring patterns and relationships within the data. The hybrid quantum-classical LSTM, which blends classical LSTM with quantum layers, offers a balance between expressiveness and stability, but in SWT application, this added complexity translated into no substantial differences in performance VQC also showed high performance, with NSE values consistently above 0.94 and KGE values above 0.93 across all stations, although it showed slightly higher MAE on average compared to the classical LSTM. The analysis suggests that the quantum variational approach may not offer additional benefits for SWT simulation over simpler classical architecture. Ultimately, the superior results of the classical LSTM highlight the importance of matching model complexity with the problems inherent in data patterns.

In addition, stations in snow-dominated and high-elevation regions, such as those located in the Upper Colorado or Pacific Northwest, showed higher accuracy across all models. This can be attributed to the strong seasonal and climatic signals in these areas, which can be easily captured by the proposed models. In contrast, stations in semi-arid or subtropical regions (e.g., west Texas) exhibited greater variability in performance, likely due to complex land–atmosphere interactions, high evaporation demand, prolonged drought conditions, and sparse forcing

Table 2
Evaluation metrics for classic LSTM, quantum-classical LSTM, QLSTM, and VQC at each USGS gauging station for the SWT simulation. The best performances are shown in bold.

Station ID	MAE				NSE				KGE			
	QLSTM	LSTM	Hybrid	VQC	QLSTM	LSTM	Hybrid	VQC	QLSTM	LSTM	Hybrid	VQC
1129200	0.551	**0.443**	0.473	0.576	0.983	**0.989**	0.987	0.982	0.976	**0.985**	0.979	0.972
1484080	0.548	0.517	**0.438**	0.532	0.993	0.994	**0.996**	0.994	0.979	0.976	0.987	**0.992**
1646305	0.716	0.675	**0.633**	0.775	0.982	**0.985**	**0.985**	0.977	0.961	0.969	**0.989**	0.979
2266300	0.594	0.46	0.482	0.492	0.958	**0.973**	0.972	0.970	0.978	**0.985**	0.977	0.983
22908295	0.695	0.624	0.656	**0.616**	0.926	**0.944**	0.939	0.940	0.946	0.954	**0.971**	0.955
3297800	1.078	**0.966**	1.057	**0.966**	0.964	**0.972**	0.965	0.971	0.942	0.957	0.952	**0.961**
3321500	0.575	0.615	**0.515**	0.519	0.992	0.992	**0.994**	0.993	0.971	0.968	0.973	**0.991**
3354000	0.902	**0.596**	0.672	0.801	0.981	**0.991**	0.989	0.985	0.958	0.983	**0.984**	**0.984**
351706800	0.927	0.731	**0.678**	0.734	0.967	0.981	**0.983**	0.979	0.946	0.949	0.95	**0.972**
4108660	0.567	**0.401**	0.441	0.518	0.994	**0.997**	0.996	0.995	0.98	**0.99**	0.981	**0.99**
4136000	0.583	0.592	**0.522**	0.632	0.989	0.989	**0.991**	0.987	0.973	0.962	0.973	**0.981**
5082500	0.545	0.431	**0.367**	0.455	0.995	**0.997**	**0.997**	**0.997**	0.994	0.976	0.992	**0.994**
5420460	0.589	0.616	0.577	**0.567**	0.995	0.994	0.995	0.995	0.975	0.967	0.979	**0.991**
6775900	0.7	**0.635**	0.689	0.783	0.975	**0.979**	0.975	0.968	**0.986**	0.981	0.97	0.984
7191222	0.756	**0.347**	0.575	0.646	0.978	**0.994**	0.986	0.983	0.958	**0.986**	0.969	0.974
7387050	0.951	0.951	**0.898**	0.907	0.964	**0.97**	**0.97**	0.963	0.954	0.948	0.923	**0.957**
8317400	0.694	0.335	**0.259**	0.261	0.988	0.997	**0.998**	**0.998**	0.95	0.977	0.987	**0.997**
8407500	0.858	1.03	0.887	**0.830**	**0.979**	0.973	0.977	**0.979**	0.968	0.942	0.936	**0.985**
9085150	0.738	**0.557**	0.563	0.566	0.98	0.988	**0.989**	0.988	0.939	0.956	**0.963**	**0.963**
9302000	0.684	**0.552**	0.616	0.841	0.991	**0.994**	0.993	0.987	0.977	**0.988**	0.973	0.964
9505800	**0.486**	0.525	0.65	0.640	**0.987**	0.986	0.98	0.980	**0.984**	0.976	0.966	0.982
10249300	0.75	**0.514**	0.597	0.715	0.965	**0.983**	0.976	0.969	0.927	**0.987**	0.94	0.937
10301500	**0.878**	0.943	1.186	0.982	**0.978**	0.975	0.962	0.973	**0.976**	0.967	0.961	**0.976**
11044000	0.424	**0.336**	0.382	0.435	0.985	**0.989**	0.988	0.985	0.973	**0.99**	0.986	0.974
11203580	0.655	**0.444**	0.547	0.602	0.977	**0.989**	0.984	0.980	0.964	**0.992**	0.98	0.958
13317660	0.486	0.525	0.349	**0.313**	0.992	0.992	**0.996**	**0.996**	0.979	0.96	**0.989**	**0.989**
295826095082200	0.52	0.526	0.524	0.491	**0.991**	**0.991**	**0.991**	**0.991**	**0.99**	0.983	0.987	**0.99**
Average	0.683	0.588	0.601	0.637	0.980	0.985	0.983	0.982	0.967	0.972	0.971	0.977

data. Despite these challenges, all models consistently yielded NSE values above 0.92 and MAE below 1.0, indicating strong performance across diverse hydroclimatic settings.

3.5. Sensitivity analysis

Since QLSTM was the best performer among the models, we performed the sensitivity analysis of QLSTM model. Also, due to superior results of SWT simulation, we only focused on the sensitivity analysis of daily streamflow results. To gain deeper insights into the predictive behavior of the QLSTM model in daily streamflow simulation, we conducted a comprehensive sensitivity analysis across the 18 zones. The QLSTM sensitivity analysis focused on six weather forcing variables: minimum temperature, vapor pressure, snow water equivalent, precipitation, maximum temperature, and solar radiation. The goal was to determine the relative importance of each variable by comparing the NSE values when all variables were included in QLSTM to those obtained when each variable was individually removed. For each zone, we calculated the average NSE value across all USGS gauging stations using all forcing inputs. We then systematically removed one variable at a time and retrained the model to obtain the corresponding average NSE. The difference between the NSE values with all forcing inputs and those with one variable excluded provided a measure of sensitivity. The difference between these two NSE values indicated that the excluded variable had a significant influence on simulation accuracy for that zone.

The results revealed considerable spatial heterogeneity in the sensitivity of input variables, consistent with climatic, topographic, and land use variations across CONUS. Sensitivity analysis further revealed that precipitation consistently emerged as the most sensitive variable influencing the accuracy of daily streamflow simulation with notable degradation in modeling performance upon its exclusion. In Mid Atlantic (zone 2) and South Atlantic-Gulf (zone 3) characterized by humid subtropical climates, densely vegetated landscapes, and frequent convective storms, the exclusion of precipitation led to a substantial decline in NSE values. The direct correlation of daily streamflow with

precipitation reflects the flashy hydrological responses and relatively small soil moisture amount in these regions. Moreover, in humid climates with relatively low topographic variability the direct relationship between rainfall and streamflow led to increasing the sensitivity of QLSTM to precipitation inputs. Table 3 summarizes the outcomes of sensitivity analysis across different zones.

In contrast, SWE provided strong control over the northern regions, particularly New England (zone 1) and Great Lakes (zone 4). These regions are characterized by humid continental and cold climate regimes with significant seasonal snow accumulation and complex freeze-thaw cycles. As a result, the NSE value declined significantly in these regions when SWE was excluded from QLSTM. The physical processes governing snowmelt-driven streamflow dominate winter and spring streamflow time series data in these regions, making SWE a significant predictor for maintaining model fidelity during transitional seasons. QLSTM, which leverages quantum superposition to enhance memory capacity, can indeed improve the encoding of information related to delays in streamflow response, especially those influenced by snowmelt processes. Both Tmin and Tmax displayed moderate, but regionally dependent, sensitivity patterns. In northern and mountainous zones, particularly Upper (zone 7) and Lower Mississippi (zone 8) regions, the exclusion of Tmin and Tmax modestly degraded QLSTM modeling performance. These results reflect the importance of temperature in modulating snowmelt rates, evapotranspiration processes, and freeze-thaw transitions that impact runoff generation mechanisms. However, in arid and semi-arid regions such as Upper and Lower Colorado (zones 14 and 15) regions, the impact of temperature variability was comparatively insignificant.

In addition, the exclusion of *vp* proved significant across the majority of hydrologic zones. For instance, in zones 3, 6, and 7, the NSE declined by approximately 0.083–0.090, while in zones 10, 11, 12, and 15, the reductions were more pronounced, ranging from 0.113 to 0.690. These declines were particularly notable in humid regions, where atmospheric moisture exerts a strong influence on evapotranspiration fluxes. In Tennessee (zone 6), characterized by humid subtropical forests, high
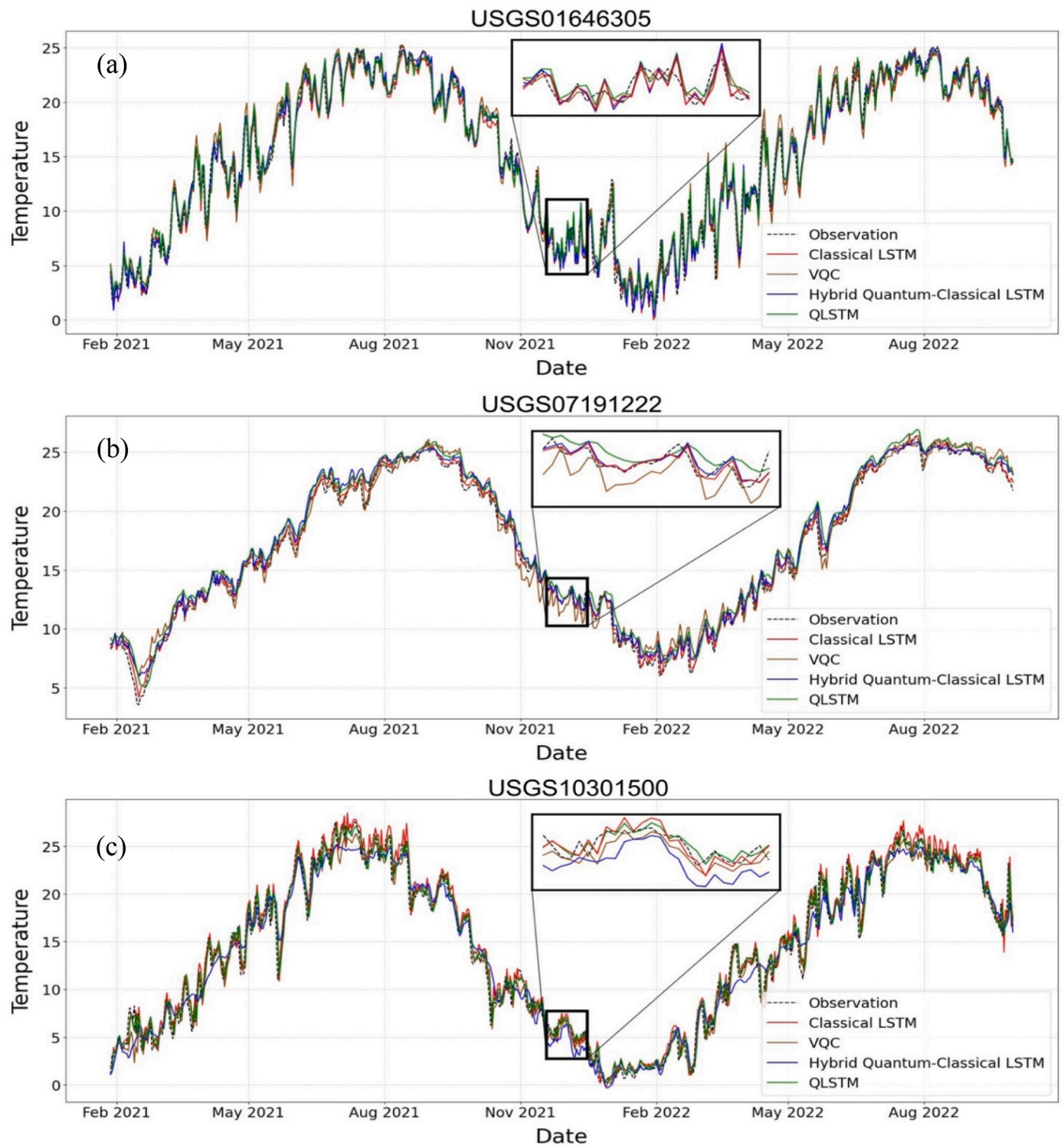
Fig. 11. Observed vs. predicted SWT at the three selected USGS monitoring sites: (a) 01646305, (b) 07191222, and (c) 10301500. Each panel displays the performance of predictive models: Classical LSTM (red), VQC (Orange), Hybrid quantum-classical LSTM (blue), and QLSTM (green), against the observed values (black dashed line). Inset plots highlight modeling performance within a fraction of time to emphasize differences. (For interpretation of the references to colour in this figure legend, the reader is referred to the Web version of this article.)

annual precipitation, and warm temperatures, the exclusion of *vp* data led to a marked reduction in model performance, indicating that vapor pressure dynamics play a critical role in regulating streamflow. Conversely, in arid basins such as the Great Basin (zone 16), the impact of *vp* exclusion was negligible, reflecting the limited contribution of atmospheric moisture to hydrological processes in regions with sparse

vegetation and minimal soil water availability.

Furthermore, the sensitivity of *srad* exhibited remarkable variability. In snow-dominated regions such as Pacific Northwest (zone 17) and California (zone 18), the removal of *srad* noticeably declined NSE values. In these zones, *srad* is the primary driver of the energy balance that can dictate snowmelt timing. For example, in snow-dominated

Table 3
Regional average NSE values based on varying sets of input variables used in QLSTM.

Zone	All Variables	Without Minimum Temperature	Without Vapor Pressure	Without Snow Water Equivalent	Without Precipitation	Without Maximum Temperature	Without Solar Radiation
1	0.586	0.598	0.594	**0.571**	0.585	0.594	0.585
2	0.445	0.431	0.439	0.435	**0.412**	0.436	0.433
3	0.561	0.454	0.471	0.441	**0.423**	0.456	0.499
4	0.783	0.780	0.776	**0.769**	0.772	0.779	0.779
5	0.531	0.512	0.527	0.516	**0.511**	0.525	0.526
6	0.565	0.508	0.482	0.500	**0.481**	0.497	0.511
7	0.522	**0.431**	0.437	0.451	0.436	0.445	0.437
8	0.686	0.661	0.679	0.702	0.657	**0.654**	0.669
9	0.948	0.936	**0.932**	0.938	0.937	0.938	0.937
10	0.678	0.581	0.565	0.574	**0.556**	0.573	0.690
11	0.367	−0.018	0.027	0.055	**−0.095**	0.122	0.047
12	−0.040	**−5.721**	−0.730	−0.851	−5.488	−5.334	−0.354
13	0.818	0.807	0.815	0.811	0.803	0.806	**0.801**
14	0.977	0.974	0.975	0.972	**0.971**	0.976	0.972
15	0.289	0.269	0.148	0.256	**0.127**	0.221	0.128
16	0.935	0.917	0.928	0.889	0.927	**0.887**	0.929
17	0.778	0.771	0.771	0.774	0.767	0.772	**0.766**
18	0.699	0.696	0.699	0.684	0.661	0.752	**0.657**

basins where *srad* drives snowmelt timing, *srad* exclusion significantly reduced NSE values. As the main driver of snowpack ablation, excluding *srad* impaired accurate snowmelt-driven streamflow simulation. While the entangled quantum memory cells of QLSTM captured delays in streamflow generation well, the performance of this algorithm declined significantly without *srad* input. In contrast, *srad* was less critical in humid tropical and subtropical basins such as Mid Atlantic (zone 2) and South Atlantic-Gulf (zone 3). Overall, the degree of sensitivity observed across regions reflects the inherent hydrological and climatic variabilities across zones. The highest sensitivity was observed in South Atlantic-Gulf (zone 3), Tennessee (zone 6), Upper Mississippi (zone 7), and Missouri (zone 10). These regions, characterized by humid climates, mixed land uses, and strong precipitation-driven streamflow regimes, which showed substantial declines in modeling performance when key climatic variables were excluded. In these regions, hydrological processes are heavily influenced by direct rainfall events, evapotranspiration dynamics, and seasonal temperature shifts, making them particularly sensitive to variations in meteorological inputs. The diverse topography and land use patterns, including agricultural activities and urbanization, further amplified their dependence on comprehensive input data to accurately predict daily streamflow values.

Conversely, regions such as Great Lakes (zone 4), Souris-Red-Rainy (zone 9), Texas-Gulf (zone 13), and Upper Colorado (zone 14), which are characterized by relatively stable hydrological regimes, demonstrated relatively low sensitivity to the exclusion of individual variables. In these regions, streamflow is less variable on a daily basis, and fluctuations of meteorological drivers such as precipitation and temperature have a direct influence on discharge patterns. Overall, QLSTM model maintained a relatively stable performance even though some input variables were excluded from the modeling run. The quantum entanglement and superposition within the hidden layers contributed to QLSTM's superior performance in capturing delayed, nonlinear, and spatially distributed hydrological processes. This was particularly evident in snow-dominated regions, where a temporal lag between meteorological forcing and hydrological response led to challenging rainfall-runoff modeling. The QLSTM's ability to maintain coherent predictive sequences despite partial input data can be attributed to the quantum encoding of temporal patterns which allows for richer representation of sequential data.

Superposition allowed the model to simultaneously evaluate multiple pathways of information flow, enhancing its ability to infer missing relationships and patterns in data when some variables were excluded. However, the sensitivity analysis revealed that while quantum features enhance model adaptability, they cannot fully offset the absence of physically dominant variables such as precipitation and SWE,

particularly in regions where streamflow is tightly driven by a single dominant process (precipitation or SWE). In addition, forested regions, such as those prevalent in Ohio (zone 5) exhibited moderate sensitivity to multiple input variables. Forested zones often feature buffered hydrological responses due to canopy interception, root zone storage, and enhanced infiltration rates. These factors mediate the influence of meteorological forcings on streamflow, resulting in a more distributed sensitivity profile. In agricultural regions such as Missouri (zone 10) and Arkansas-White-Red (zone 11) which are characterized by extensive land modification and artificial drainage networks, the sensitivity of QLSTM to precipitation remained significant. Rapid surface runoff generation in agricultural basins boosted the model's confidence in precipitation inputs for effective daily streamflow simulation. The QLSTM model capitalized on these moderated dynamics by maintaining relatively stable predictive performance even though certain variables were excluded.

Overall, the sensitivity of QLSTM varied significantly across CONUS, underscoring differences in hydrological responses. In regions with rapid hydrological response to precipitation, such as humid tropical zones (zone 3), streamflow generation is tightly associated with meteorological conditions. In contrast, the sensitivity results for snow-dominated or groundwater-dominated basins with longer hydrological responses showed more distributed sensitivity patterns, reflecting the integration of antecedent soil conditions over a longer timeframe. The ability of QLSTM to encode long-term dependencies using quantum entanglement enhanced its performance in these basins with prolonged hydrological response times.

3.6. Model generalization across regions

In continuation of our analyses, the capability of the models was further assessed for generalization across different gauging stations within the same zone. Within each zone, we initially selected a representative group of stations based on factors like spatial distribution, land use, etc. Consequently, a random sample of 10 stations was selected if the zone contained 10 or more, or a complete set of stations if fewer than 10 were present. This selected set of stations for each zone was then randomly divided, allocating 70 % of the gauging stations for model training and the remaining 30 % for testing. The classical LSTM, VQC, hybrid quantum-classical LSTM, and QLSTM models were trained using data solely from the designated training stations. The predictive performance of the models was then evaluated on the unseen stations from the same zone during testing period. Table 4 summarizes the results of generalization performance, presenting the average NSE, MAE, and KGE values for each zone.

Table 4

modeling generalization across testing stations within each zone for all models. Metrics are computed over the testing period using unseen stations. The best performances are shown in bold.

Zone	Classical LSTM			Hybrid quantum-classical LSTM			QLSTM			VQC		
	NSE	MAE	KGE	NSE	MAE	KGE	NSE	MAE	KGE	NSE	MAE	KGE
1	0.64	48.2	0.71	0.68	41.93	**0.79**	**0.73**	**37.4**	0.77	0.65	63.2	0.68
2	0.24	68.3	0.48	0.14	98.83	0.21	0.21	118	0.05	**0.44**	**53.7**	**0.51**
3	0.32	**39.8**	**0.38**	0.31	51.48	0.34	0.31	47.9	0.36	**0.35**	44.8	0.34
4	**0.98**	**18.4**	**0.94**	0.97	22.32	0.93	0.97	20	0.92	0.96	31.7	0.93
5	0.47	24.5	0.6	0.42	27.32	0.52	0.48	**24.3**	0.64	**0.55**	49.9	**0.65**
6	**0.57**	128	**0.58**	0.52	158.3	0.49	0.51	158	0.46	0.4	139	0.38
7	0.58	**100**	0.58	0.49	108	0.55	0.49	123	0.38	**0.77**	133	**0.74**
8	0.46	402	0.63	0.47	366.7	0.61	0.41	429	0.63	**0.84**	**100**	**0.87**
9	**0.99**	71.9	0.93	**0.99**	**67.03**	**0.94**	0.98	79.5	0.93	0.95	222	0.94
10	0.76	13.9	**0.88**	0.69	16.99	0.72	**0.78**	12.7	0.87	0.61	**3.74**	0.63
11	**0.49**	84.6	**0.36**	0.46	92.35	0.32	0.47	118	0.16	−2.8	**9.38**	−1.4
12	−1.4	79.3	−0.3	−0.8	67.25	−1.8	−2.7	110	−3.8	−16	117	−2.6
13	**0.54**	**5.09**	**0.74**	0.52	5.69	0.71	0.5	5.86	**0.74**	0.41	10.2	0.33
14	0.98	7.96	0.95	0.98	8.62	0.94	**0.99**	**7.28**	**0.97**	0.98	18.8	0.96
15	**0.3**	23.2	**0.64**	0.03	35.82	−0.6	0.22	**20.9**	0.21	0.14	30.6	0.09
16	0.93	4.27	0.92	0.93	**3.74**	**0.94**	**0.94**	3.95	0.92	0.88	3.99	0.71
17	**0.5**	**139**	0.69	0.32	162.6	0.59	0.5	156	0.66	0.48	218	**0.73**
18	**0.62**	**203**	**0.75**	0.51	361.7	0.4	0.56	308	0.56	0.53	775	0.73

The results revealed significant variability in the capability of classical LSTM, VQC, hybrid quantum-classical LSTM, and QLSTM models to generalize daily streamflow simulations within each zone. The results showed that there isn't a single model that consistently outperforms the others across all zones for streamflow generalization. The classical LSTM model demonstrated the best generalization performance in zones 3, 4, 6, 7, 11, 13, 17 and 18 consistently outperforming the other models across all evaluation metrics. In addition, QLSTM and VQC outperformed other models in zone 1, 2, 5,7, 8 and 14, which implies the quantum algorithms are highly capable of modeling complex data. It is important to note that the QLSTM used in this study was designed with only 4 qubits while VQC was designed with 8 qubits, hence a QLSTM contained a significantly small number of training parameters compared to classic and hybrid LSTM models. The classical quantum hybrid model was the top performer in only zones 9 and 16. The results revealed that the variability in hydrological characteristics, data complexity, and patterns within each zone significantly influenced the selection of the most appropriate model for that specific region. In snow-dominated and high-elevation regions, models exhibited strong spatial dependencies, particularly in Great Lakes (zone 4), Souris-Red-Rainy (zone 9), Upper Colorado (zone 14), and Great Basin (zone 16), where NSE and KGE scores consistently approached near-perfect values. These results revealed that the models are proficient in regions characterized by pronounced, predictable snowmelt-driven streamflow. Conversely, eastern zones displayed more mixed results. Moderate generalization was observed in New England (zone 1), where QLSTM notably outperformed the other models. However, in the Mid-Atlantic region (zone 2), all models struggled equally, indicating that the complexity introduced by varying physiographic settings and urbanization can challenge daily streamflow simulation. Meanwhile, excellent generalization was observed in the Great Lakes region (zone 4), suggesting that moderate climatic conditions influenced by the lakes facilitated more uniform hydrological responses. Regions such as Ohio (zone 5), Tennessee (zone 6), and Upper Mississippi (zone 7) showed moderate performance, highlighting the impacts of mixed land use, regulated river systems, and snowmelt patterns on streamflow variability. In contrast, zones 9 (Souris-Red-Rainy) and 10 (Missouri Region) exhibited strong generalization across all models.

In the southern and central U.S., the generalization results varied widely. Performance in highly diverse and heterogeneous regions such as the South Atlantic-Gulf (zone 3) and Lower Mississippi (zone 8) were notably poor due to complexities in precipitation patterns, engineered water management systems, and complex streamflow patterns. The Arkansas-White-Red (zone 11) and Texas-Gulf (zone 12) basins demonstrated similar challenges because of erratic precipitation patterns with significant effects on the hydrological cycle. The Rio Grande (zone 13) responded positively to generalization with moderate NSE, high KGE, and low MAE, likely due to consistency in streamflow data and snow equivalent water effect on simulations.

Western basins, on the other hand, presented mixed performance reflective of their unique topographic and climatic diversity. Low generalization was observed in the highly regulated basins such as Lower Colorado basin (HUC 15), where altered flow regimes complicated streamflow simulation. Zones 14 (Upper Colorado) and 16 (Great Basin), however, demonstrated strong generalization performance, indicating a high degree of predictability in these snowmelt-dominated regions. The Pacific Northwest (zone 17) and California (zone 18) basins displayed moderate NSE but high MAE values, suggesting significant challenges in accurately simulating flow magnitudes across diverse hydroclimatic regions. California's complex hydrologic system, shaped by snowpack variability and intensive regulation hindered simulation performance.

Overall, generalization was mostly successful in regions characterized by uniform hydrological drivers, primarily snowmelt and moderate climatic conditions, while significant challenges arose in regions with complex hydrological systems, extensive human interventions, and substantial climatic variability. The findings emphasize that when selecting a quantum-driven model for a hydrologic simulation task, it's crucial to ensure the model generalizes well to new, unseen data and to consider specific regional characteristics. This means the model should not only perform well on the training data but also be adaptable to different situations and datasets, and that the chosen model's attributes should align with the specific characteristics of the new region.

3.7. Computational cost

The results demonstrated a significant difference in computational cost. The training time of QLSTM was around 139.4 s per epoch which is substantially higher than other models. In contrast, the hybrid quantum-classical LSTM was the most efficient at 2.43 s, while the classic LSTM and the VQC required 2.65 s and 3.83 s, respectively. The difference in computational cost between the classic LSTM and the VQC is primarily due to the overhead simulating quantum circuits on classical hardware. The default qubit backend tracks the full state vector of the qubits, a method known to be computationally intensive. Technically, the cost of state vector simulation scales exponentially with the number of qubits.

Therefore, even with the relatively small 4-qubit circuits used in this study, the simulation was time-consuming. This specific choice was a balance between model capacity and computational feasibility. The number of qubits directly influences the expressiveness of the quantum circuit; however, simulating quantum circuits on classical hardware incurs an exponential cost in memory and computation time with each additional qubit. A 4-qubit system, representing a 16-dimensional state space, provided a sufficiently complex circuit architecture to capture non-linear hydrological relationships while remaining computationally tractable for the large-scale benchmarking performed across hundreds of catchments. The performance gap can possibly widen dramatically for more complex circuits involving a larger number of qubits. It is important to note that the bottleneck in performance and qubit count arises from simulating quantum operations on classical hardware, rather than being an inherent limitation of the quantum algorithms. When implemented on native quantum hardware, these algorithms are expected to run significantly faster and scale to far more qubits, potentially yielding improved results.

4. Conclusion and future work

This study developed a new Python package called HydroQuantum for hydrological simulations. The package includes QLSTM, VQC, and hybrid quantum-classical LSTM that are tested for daily streamflow and SWT simulations across CONUS. Through extensive computational experiments and rigorous sensitivity analysis, our results revealed compelling evidence of the potential advantages and inherent limitations of quantum-enhanced neural networks in hydrological simulations. The comprehensive performance assessment highlighted the distinctive strengths inherent in quantum-enhanced architecture. First, the selection of quantum-driven models for daily streamflow simulations should be tailored to basin-specific characteristics and management regimes. Second, QLSTM exhibits certain strengths relative to classical LSTM, primarily due to its ability to leverage quantum mechanical principles. This includes enhanced memory capacity, improved handling of long-range dependencies, and greater expressive power for complex time-series data. Quantum strength arises from superposition and entanglement, embedded within the VQCs to achieve enhanced efficiency in handling temporal dependencies. This quantum parallelism, made possible by these quantum phenomena, allows QLSTMs to process information in a way that classical LSTMs cannot, potentially leading to faster and more accurate handling of complex temporal patterns in data.

Moreover, entanglement facilitates correlated quantum states across qubits, offering enhanced capability for capturing interdependencies and non-linear interactions among hydrological variables, which are notoriously challenging for classical LSTM to accurately replicate. Superposition, which allows qubits to represent multiple states simultaneously, significantly enhanced the representational power of the classical LSTM by concurrently exploring multiple possible model states. Our findings highlight that integrating quantum-inspired mechanisms into LSTM architecture can improve predictive accuracy, particularly in basins prone to extreme hydrological events or regulated-flow conditions. Furthermore, the quantum computational approach enhanced temporal encoding capabilities of the model which was especially beneficial in snow-dominated regions, such as the Great Lakes and Upper Colorado basins. In these basins, hydrological responses are primarily driven by snow accumulation and subsequent melt processes which exhibit complex, temporal patterns and delayed responses to streamflow generation. QLSTM demonstrated enhanced predictive capabilities due to its intrinsic ability to encode these delayed and nonlinear interactions, showing improvements relative to classical LSTM.

In addition, the hybrid quantum-classical LSTM, integrating classical LSTM layers with quantum-enhanced circuits, showed competitive performance, demonstrating its ability in simulating complex data

patterns in daily streamflow time series. The hybrid quantum-classical LSTM leverages classical LSTM's sophisticated memory mechanism to process sequential data to capture long-term dependencies. This algorithm also benefits from the quantum circuits' ability to capture intricate and subtle temporal dynamics via superposition and entanglement. These strengths proved particularly advantageous in complex and regulated basins characterized by heterogeneous precipitation patterns, diverse land-use changes, and considerable anthropogenic climatic change. Here, hybrid quantum-classical LSTM capability for spatial generalization and its balanced representation of bias, correlation, and variability underscore its practical applications for both streamflow and SWT simulations.

Overall, QLSTM showcased substantial predictive improvements in complex daily streamflow simulations, while the performance of this algorithm diminished for time series data with regular trends such as SWT. All models demonstrated strong performance for SWT simulation with insignificant differences observed among them. The classical LSTM showed better results by efficiently capturing the dynamics of SWT data. Although the hybrid quantum-classical LSTM and QLSTM maintained robust performances, their quantum enhancements provided no substantial improvements in SWT simulation. This finding underscores the importance of appropriately matching model complexity with time series patterns, suggesting that quantum computational advantages might not technically justify their computational costs and complexities unless they deal with highly complex hydrological time series data.

Sensitivity analysis of QLSTM revealed significant variability in the sensitivity of streamflow simulation to different meteorological inputs across CONUS. Quantum models, despite their advanced temporal modeling capabilities, remain dependent on accurate, complete, and physically meaningful input data. The results demonstrated that integrating sensitivity assessments into the quantum workflow is essential for developing robust, geographically tailored hydrologic simulation. Furthermore, sensitivity results can inform data collection priorities, suggesting which meteorological variables require higher spatial and temporal resolution in measurements to enhance streamflow simulations in specific regions. Incorporating such insights into future modeling designs can contribute to more resilient and informed river system management under non-stationarity.

Moreover, modeling generalization across different gauging stations within each zone revealed substantial variability in performance metrics. Classic LSTM exhibited robust generalization, particularly excelling in diverse contexts such as snow-dominated and regulated basins. QLSTM showed superior performance in regions such as New England, underscoring its strength in modeling intricate temporal patterns through quantum superposition and entanglement. In addition, the hybrid quantum-classical LSTM performed well in the Lower Mississippi and Great Basin but was generally less effective than the classical and QLSTM. Regions characterized by extreme events and high complexity such as eastern basins and highly regulated western basins, posed significant challenges for all models. These findings emphasize that model selection should be guided by specific regional hydrological attributes and flow regimes, reinforcing the necessity of tailored modeling strategies for effective hydrological simulation.

When considering the practical significance of these results, it is important to note that although some quantum-driven models did not consistently outperform the classical LSTM in every scenario, their relative improvements in critical metrics (e.g., NSE, KGE) across multiple hydroclimatic zones suggest region-specific advantages. The practical significance of this work lies in demonstrating the feasibility and adaptability of quantum-enhanced architectures in hydrological simulations, especially in regions characterized by nonlinear, delayed, or peak-dominated flow dynamics. Moreover, this study provides the first large-scale benchmarking of QLSTM, VQC, and hybrid quantum-classical models on hydrologic datasets, laying the groundwork for future improvements as quantum hardware advances. By establishing baseline performance, this research offers a valuable reference point for

subsequent quantum-hydrologic model development.

Despite the considerable promise and theoretical advantages demonstrated herein, quantum-enhanced models are not without significant limitations and practical challenges. One primary limitation involves computational complexity and resource demands associated with simulating quantum computations on classical hardware. Current quantum computing hardware remains at an early stage of development, lacking sufficient qubit numbers, coherence times, and error rates required for practical, large-scale applications. Consequently, the present study employed quantum simulations executed on classical computational resources, inherently limiting scalability and efficiency. Furthermore, quantum circuit optimization, a critical step in training quantum neural networks, remains challenging due to the phenomena of barren plateaus, a scenario where gradients vanish exponentially as quantum circuit depth increases. This challenge arises because the exponentially growing quantum state space, combined with random initialization of quantum circuits that can lead to landscapes where gradients are vanishingly small.

Overall, the exploration of quantum-enhanced neural network architectures demonstrated substantial promises for improving hydrological simulation. Although, the realization of quantum computing application in hydrological simulation necessitates overcoming significant quantum computational challenges, including hardware limitations, optimization complexities, and computational scalability. Future research focusing on quantum algorithm refinement, quantum hardware advancements, and hybrid quantum-classical integration is crucial to unlock the full potential of quantum-enhanced neural networks for various hydrological applications. This approach will enable more efficient and powerful solutions for complex hydrological simulation problems that are currently intractable for classical neural networks. Integrating these quantum algorithms into HydroQuantum Python package, streamlines quantum computing development for hydrologic simulations. HydroQuantum allows developers to leverage quantum algorithms for hydrological simulations, making quantum computing more accessible for hydrological applications. HydroQuantum package is anticipated to significantly enhance the efficiency, scalability, and performance of quantum-driven hydrological simulation.

CRediT authorship contribution statement

Mostafa Saberian: Writing – original draft, Validation, Software, Formal analysis, Data curation. **Nima Zafarmomen:** Writing – original draft, Visualization, Validation, Software, Methodology, Formal analysis, Data curation. **Adarsha Neupane:** Writing – original draft, Visualization, Validation, Software, Formal analysis, Data curation. **Krishna Panthi:** Writing – original draft, Visualization, Validation, Software, Formal analysis, Data curation. **Vidya Samadi:** Writing – review & editing, Validation, Supervision, Software, Resources, Project administration, Methodology, Investigation, Funding acquisition, Formal analysis, Conceptualization.

Software availability

Name of packages: HydroQuantum.
Developers: Mostafa Saberian, Nima Zafarmomen, Adarsha Neupane, Krishna Panthi, and Vidya Samadi.
Date first available: June 15, 2025.
Package Availability: The package will be available after publication.
License: MIT License.
Software requirements: pandas, numpy, torch, sklearn, pennylane, matplotlib, and CUDA-enabled PyTorch for GPU acceleration.
Hardware requirements: CPU: Multi-core processor (e.g., Intel i5 or equivalent), RAM: 8 GB, and Storage: 500 MB for package and dependencies, additional space for data. CPU: High-performance multi-core processor (e.g., Intel i7 or AMD Ryzen), RAM: 16 GB or more, GPU:

NVIDIA GPU with CUDA support (e.g., GTX 1060 or higher) for accelerated PyTorch computations, and Storage: SSD with at least 1 GB for faster data processing.

Data availability

CAMLES data is available https://ral.ucar.edu/solutions/products/camels. SWT data is available at https://waterwatch.usgs.gov/wqwatch/

References

Addor, N., Newman, A.J., Mizukami, N., Clark, M.P., 2017. The CAMELS data set: catchment attributes and meteorology for large-sample studies. Hydrol. Earth Syst. Sci. 21 (10), 5293–5313. https://doi.org/10.5194/hess-21-5293-2017.

Arnold, J.G., Srinivasan, R., Muttiah, R.S., Williams, J.R., 1998. Large area hydrologic modeling and assessment part I: model DEVELOPMENT[1]. JAWRA Journal of the American Water Resources Association 34 (1), 73–89. https://doi.org/10.1111/j.1752-1688.1998.tb05961.x.

Bartholow, J.M., 1989. Stream temperature investigations: field and analytical methods. In: US Fish and Wildlife 815 Service, vol. 89. Retrieved from. https://www.krisweb.com/biblio/gen_usfws_bartholow_1989_br8917.pdf.

Bergholm, V., Izaac, J., Schuld, M., Gogolin, C., Ahmed, S., Ajith, V., et al., 2018. Pennylane: automatic differentiation of hybrid quantum-classical computations. arXiv. https://doi.org/10.48550/arXiv.1811.04968 preprint arXiv:1811.04968.

Bergström, S., 1976. Development and application of a conceptual runoff model for Scandinavian catchments.

Beven, K.J., Kirkby, M.J., 1979. A physically based, variable contributing area model of basin hydrology / Un modèle à base physique de zone d'appel variable de l'hydrologie du bassin versant. Hydrological Sciences Bulletin 24 (1), 43–69. https://doi.org/10.1080/02626667909491834.

Biamonte, J., Wittek, P., Pancotti, N., et al., 2017. Quantum machine learning. Nature 549, 195–202. https://doi.org/10.1038/nature23474.

Bicknell, B.R., Imhoff, J.C., Kittle Jr., J.L., Donigian Jr., A.S., Johanson, R.C., 1997. Hydrological simulation program—FORTRAN user's manual for version 11. Environmental Protection Agency Report No. EPA/600/R-97/080. US Environmental Protection Agency, Athens, Ga.

Bosompemaa, P., Brookfield, A., Zipper, S., Hill, M.C., 2025. Using national hydrologic models to obtain regional climate change impacts on streamflow basins with unrepresented processes. Environ. Model. Software 183, 106234. https://doi.org/10.1016/j.envsoft.2024.106234.

Chen, S.Y.C., Yang, C.H.H., Qi, J., Chen, P.Y., Ma, X., Goan, H.S., 2020. Variational quantum circuits for deep reinforcement learning. IEEE Access 8, 141007–141024. https://doi.org/10.1109/ACCESS.2020.3010470.

Chen, S.Y.-C., Yoo, S., Fang, Y.-L.L., 2022. Quantum long short-term memory. In: ICASSP 2022 - 2022 IEEE International Conference on Acoustics, Speech and Signal Processing (ICASSP), pp. 8622–8626. https://doi.org/10.1109/ICASSP43922.2022.9747369.

Chen, Y.D., Carsel, R.F., McCutcheon, S.C., Nutter, W.L., 1998. Stream temperature simulation of forested riparian areas: I. Watershed-Scale model development. J. Environ. Eng. 124 (4), 304–315. https://doi.org/10.1061/(ASCE)0733-9372(1998)124:4(304).

Dehghani, A., Moazam, H.M.Z.H., Mortazavizadeh, F., Ranjbar, V., Mirzaei, M., Mortezavi, S., Ng, J.L., Dehghani, A., 2023. Comparative evaluation of LSTM, CNN, and ConvLSTM for hourly short-term streamflow forecasting using deep learning approaches. Ecol. Inform. 75, 102119. https://doi.org/10.1016/j.ecoinf.2023.102119.

Dutta, S., Innan, N., Yahia, S.B., Shafique, M., 2024. AQ-PINNs: attention-enhanced quantum physics-informed neural networks for carbon-efficient climate modeling (No. arXiv:2409.01626). arXiv. https://doi.org/10.48550/arXiv.2409.01626.

Fathian, F., Mehdizadeh, S., Kozekalani Sales, A., Safari, M.J.S., 2019. Hybrid models to improve the monthly river flow prediction: integrating artificial intelligence and non-linear time series models. J. Hydrol. 575, 1200–1213. https://doi.org/10.1016/j.jhydrol.2019.06.025.

Forcer, T.M., Hey, A.J.G., Ross, D.A., Smith, P.G.R., 2002. Superposition, entanglement and Quantum computation. Quant. Inf. Comput. 2 (2), 97–116. https://doi.org/10.26421/QIC2.2-1.

Gers, F.A., Schmidhuber, J., Cummins, F., 2000. Learning to forget: continual prediction with LSTM. Neural Comput. 12 (10), 2451–2471. https://doi.org/10.1162/089976600300015015.

Ghimire, S., Yaseen, Z.M., Farooque, A.A., Deo, R.C., Zhang, J., Tao, X., 2021. Streamflow prediction using an integrated methodology based on convolutional neural network and long short-term memory networks. Sci. Rep. 11 (1), 17497. https://doi.org/10.1038/s41598-021-96751-4.

Gochis, D.J., Yu, W., Yates, D.N., 2015. The WRF-Hydro model technical description and user's guide, version 3.0. NCAR Tech. Doc. 120. Available online at: http://www.ral.ucar.edu/projects/wrf_hydro/.

Graf, R., Aghelpour, P., 2021. Daily River water temperature prediction: a comparison between neural network and stochastic techniques. Atmosphere 12 (9). https://doi.org/10.3390/atmos12091154. Article 9.

Hamlet, A.F., Huppert, D., Lettenmaier, D.P., 2002. Economic value of long-lead streamflow forecasts for Columbia River hydropower. J. Water Resour. Plann. Manag. 128 (2), 91–101. https://doi.org/10.1061/(ASCE)0733-9496(2002)128:2 (91.

Hani, I., St-Hilaire, A., Ouarda, T.B.M.J., 2023. Machine-learning modeling of hourly potential thermal refuge area: a case study from the Sainte-Marguerite River (Quebec, Canada). River Res. Appl. 39 (9), 1763–1782. https://doi.org/10.1002/rra.4191.

He, E., Xie, Y., Sun, A., Zwart, J., Yang, J., Jin, Z., Wang, Y., Karimi, H., Jia, X., 2024. Fair graph learning using constraint-aware priority adjustment and graph masking in river networks. In: Proceedings of the AAAI Conference on Artificial Intelligence, vol. 38, pp. 22087–22095. https://doi.org/10.1609/aaai.v38i20.30212, 20.

Hochreiter, S., Schmidhuber, J., 1997. Long short-term memory. Neural Comput. 9 (8), 1735–1780. https://doi.org/10.1162/neco.1997.9.8.1735. Neural Computation.

Innan, N., Marchisio, A., Bennai, M., Shafique, M., 2024. *LEP-QNN: loan eligibility prediction using Quantum neural networks* (No. arXiv:2412.03158). arXiv. https://doi.org/10.48550/arXiv.2412.03158.

Khan, M.A., Aman, M.N., Sikdar, B., 2024. Beyond bits: a review of quantum embedding techniques for efficient information processing. IEEE Access 12, 46118–46137. https://doi.org/10.1109/ACCESS.2024.3382150.

Kingma, D.P., 2014. Adam: a method for stochastic optimization. arXiv. https://doi.org/10.48550/arXiv.1412.6980 preprint arXiv:1412.6980.

Kratzert, F., Klotz, D., Brenner, C., Schulz, K., Herrnegger, M., 2018. Rainfall–runoff modelling using Long Short-term memory (LSTM) networks. Hydrol. Earth Syst. Sci. 22, 6005–6022. https://doi.org/10.5194/hess-22-6005-2018.

Lei, H., Li, H., Hu, W., 2024. Enhancing the streamflow simulation of a process-based hydrological model using machine learning and multi-source data. Ecol. Inform. 82, 102755. https://doi.org/10.1016/j.ecoinf.2024.102755.

Lin, Y., Wang, D., Meng, Y., Sun, W., Qiu, J., Shangguan, W., Cai, J., Kim, Y., Dai, Y., 2023. Bias learning improves data driven models for streamflow prediction. J. Hydrol.: Reg. Stud. 50, 101557. https://doi.org/10.1016/j.ejrh.2023.101557.

Mohammadi, K., Eslami, H.R., Kahawita, R., 2006. Parameter estimation of an ARMA model for river flow forecasting using goal programming. J. Hydrol. 331 (1–2), 293–299. https://doi.org/10.1016/j.jhydrol.2006.05.017.

Neupane, A., Sawada, Y., 2023. Performance assessment of irrigation projects in Nepal by integrating landsat images and local data. Remote Sens. 15 (18), 4633. https://doi.org/10.3390/rs15184633.

Newman, A.J., Clark, M.P., Sampson, K., Wood, A., Hay, L.E., Bock, A., et al., 2015. Development of a large-sample watershed-scale hydrometeorological data set for the contiguous USA: data set characteristics and assessment of regional variability in hydrologic model performance. Hydrol. Earth Syst. Sci. 19 (1), 209–223. https://doi.org/10.5194/hess-19-209-2015.

Newman, A.J., Mizukami, N., Clark, M.P., Wood, A.W., Nijssen, B., Nearing, G., 2017. Benchmarking of a physically based hydrologic model. Journal of Hydrometeorology 18 (8), 2215–2225. https://doi.org/10.1175/JHM-D-16-0284.1.

Nielsen, M.A., Chuang, I.L., 2010. Quantum Computation and Quantum Information. Cambridge university press. https://doi.org/10.1017/CBO9780511976667.

Okewu, E., Misra, S., Maskeliūnas, R., Damaševičius, R., Fernandez-Sanz, L., 2017. Optimizing green computing awareness for environmental sustainability and economic security as a stochastic optimization problem. Sustainability 9 (10). https://doi.org/10.3390/su9101857. Article 10.

Oppel, H., Schumann, A.H., 2020. Machine learning based identification of dominant controls on runoff dynamics. Hydrol. Process. 34 (11), 2450–2465. https://doi.org/10.1002/hyp.13740.

Paszke, A., Gross, S., Massa, F., Lerer, A., Bradbury, J., Chanan, G., et al., 2019. Pytorch: an imperative style, high-performance deep learning library. Adv. Neural Inf. Process. Syst. 32. https://doi.org/10.48550/arXiv.1912.01703.

Pianosi, F., Wagener, T., 2015. A simple and efficient method for global sensitivity analysis based on cumulative distribution functions. Environ. Model. Software 67, 1–11. https://doi.org/10.1016/j.envsoft.2015.01.004.

Rahmani, F., Shen, C., Oliver, S., Lawson, K., Appling, A., 2021. Deep learning approaches for improving prediction of daily stream temperature in data-scarce, unmonitored, and dammed basins. Hydrol. Process. 35 (11), e14400. https://doi.org/10.1002/hyp.14400.

Saberian, M., Samadi, V., Popescu, I., 2024. Probabilistic hierarchical interpolation and interpretable configuration for flood prediction. Hydrol. Earth Syst. Sci. Discuss. 1–41. https://doi.org/10.5194/hess-2024-261.

Sadler, J.M., Appling, A.P., Read, J.S., Oliver, S.K., Jia, X., Zwart, J.A., Kumar, V., 2022. Multi-Task deep learning of daily streamflow and water temperature. Water Resour. Res. 58 (4), e2021WR030138. https://doi.org/10.1029/2021WR030138.

Sai, S., Sen, A., Mallick, C., Mallik, A., Sen, U., Paul, M., Sutradhar, A., Roy, S., 2024. QGAPHnet: Quantum Genetic Algorithm Based Hybrid QLSTM Model for Soil Moisture Estimation. IGARSS 2024 - 2024 IEEE International Geoscience and Remote Sensing Symposium 5191–5194. https://doi.org/10.1109/IGARSS53475.2024.10641651.

Sakhuja, S., Siyanwal, S., Tiwari, A., Britant, Kashyap, S., 2025. Quantum-Assisted Machine Learning Models for Enhanced Weather Prediction (No. arXiv:2503.23408). https://doi.org/10.48550/arXiv.2503.23408.

Samadi, V., Fowler, H.J., Lamond, J., Wagener, T., Brunner, M., Gourley, J., et al., 2025. The needs, challenges, and priorities for advancing global flood research. Wiley Interdisc. Rev.: Water 12 (3), e70026. https://doi.org/10.1002/wat2.70026.

Simoes, R.D.M., Huber, P., Meier, N., Smailov, N., Fuchslin, R.M., Stockinger, K., 2023. Experimental evaluation of Quantum machine learning algorithms. IEEE Access 11, 6197–6208. https://doi.org/10.1109/ACCESS.2023.3236409.

Sun, A.Y., Jiang, P., Mudunuru, M.K., Chen, X., 2021. Explore spatio-temporal learning of large sample hydrology using graph neural networks. Water Resour. Res. 57 (12), e2021WR030394. https://doi.org/10.1029/2021WR030394.

Tabas, S.S., Samadi, S., 2022. Variational Bayesian dropout with a Gaussian prior for recurrent neural networks application in rainfall–runoff modeling. Environ. Res. Lett. 17 (6), 065012. https://doi.org/10.1088/1748-9326/ac7247.

Tan, Q.-F., Lei, X.-H., Wang, X., Wang, H., Wen, X., Ji, Y., Kang, A.-Q., 2018. An adaptive middle and long-term runoff forecast model using EEMD-ANN hybrid approach. J. Hydrol. 567, 767–780. https://doi.org/10.1016/j.jhydrol.2018.01.015.

Thornton, P.E., Thornton, M.M., Mayer, B.W., Wei, Y., Devarakonda, R., Vose, R.S., Cook, R.B., 2016. Daymet: daily surface weather data on a 1-km grid for North America, version 3. ORNL DAAC, Oak Ridge, Tennessee, USA. USDA-NASS, 2019. 2017 Census of Agriculture, Summary and State Data, Geographic Area Series, Part 51, AC-17-A 51. https://doi.org/10.3334/ORNLDAAC/1328.

Ulaski, M.E., Warkentin, L., Naman, S.M., Moore, J.W., 2023. Spatially variable effects of streamflow on water temperature and thermal sensitivity within a salmon-bearing watershed in interior British Columbia, Canada. River Res. Appl. 39 (10), 2036–2047. https://doi.org/10.1002/rra.4200.

Umutoni, L., Samadi, V., Vellidis, G., Privette III, C., Payero, J., Koc, B., 2025. Decoding time: unraveling the power of N-BEATS and N-HiTS vs. LSTM for accurate soil moisture prediction. Comput. Electron. Agric. 237, 110614. https://doi.org/10.1016/j.compag.2025.110614.

USGS WaterWatch, 2025. WaterWatch toolkit. U. S. Geological Survey. https://waterwatch.usgs.gov/index.php?id=ww_toolkit. Accessed on 6/12/2025.

Vliet, M.T., Yearsley, J.R., Franssen, W.H.P., Ludwig, F., Haddeland, I., Lettenmaier, D. P., Kabat, P., 2012. Coupled daily streamflow and water temperature modelling in large river basins. Hydrol. Earth Syst. Sci. 16 (11), 4303–4321. https://doi.org/10.5194/hess-16-4303-2012.

Wang, R., Gentine, P., Yin, J., Chen, L., Chen, J., Li, L., 2021. Long-term relative decline in evapotranspiration with increasing runoff on fractional land surfaces. Hydrol. Earth Syst. Sci. 25 (7), 3805–3818. https://doi.org/10.5194/hess-25-3805-2021.

Wang, Y., 2012. Quantum computation and Quantum information. Stat. Sci. 27 (3). https://doi.org/10.1214/11-STS378.

Wen, X., Feng, Q., Deo, R.C., Wu, M., Yin, Z., Yang, L., Singh, V.P., 2019. Two-phase extreme learning machines integrated with the complete ensemble empirical mode decomposition with adaptive noise algorithm for multi-scale runoff prediction problems. J. Hydrol. 570, 167–184. https://doi.org/10.1016/j.jhydrol.2018.12.060.

Windheuser, L., Karanjit, R., Pally, R., Samadi, S., Hubig, N.C., 2023. An end-to-end flood stage prediction system using deep neural networks. Earth Space Sci. 10 (1). https://doi.org/10.1029/2022EA002385 p.e2022EA002385.

Xia, Y., Ek, M.B., Peters-Lidard, C.D., Mocko, D., Svoboda, M., Sheffield, J., Wood, E.F., 2014. Application of USDM statistics in NLDAS-2: optimal blended NLDAS drought index over the continental United States. J. Geophys. Res. Atmos. 119 (6), 2947–2965. https://doi.org/10.1002/2013JD020994.

Xu, Z., Yu, W., Zhang, C., Chen, Y., 2024. Quantum convolutional long short-term memory based on variational quantum algorithms in the era of NISQ. Information 15 (4). https://doi.org/10.3390/info15040175. Article 4.

Yu, X., Zhang, X., Qin, H., 2018. A data-driven model based on Fourier transform and support vector regression for monthly reservoir inflow forecasting. J. Hydro-Environ. Res 18, 12–24. https://doi.org/10.1016/j.jher.2017.10.005.

Zafarmomen, N., Samadi, V., 2025. Can large language models effectively reason about adverse weather conditions? Environ. Model. Software 188, 106421. https://doi.org/10.1016/j.envsoft.2025.106421.

Zafarmomen, N., Alizadeh, H., Bayat, M., Ehtiat, M., Moradkhani, H., 2024. Assimilation of sentinel-based leaf area index for modeling surface-ground water interactions in irrigation districts. Water Resour. Res. 60 (10), e2023WR036080. https://doi.org/10.1029/2023WR036080.

Zhou, Y., Xu, C.C., Song, M., Wong, Y.K., Du, K., 2024. A novel quantum LSTM network (No. arXiv:2406.08982; version 1). arXiv. https://doi.org/10.48550/arXiv.2406.08982.